

Coordinated 1996 HST and IRTF Imaging of Neptune and Triton

II. Implications of Disk-Integrated Photometry¹

L. A. Sromovsky² and P. M. Fry

Space Science and Engineering Center, University of Wisconsin, Madison, Wisconsin 53706
E-mail: larry.sromovsky@ssec.wisc.edu

K. H. Baines²

Jet Propulsion Laboratory, California Institute of Technology, Pasadena, California 91109

and

T. E. Dowling

Comparative Planetology Laboratory, University of Louisville, Louisville, Kentucky 40292

Received July 15, 1999; revised October 17, 2000

Near-IR groundbased observations coordinated with Wide Field Planetary Camera 2 (WFPC2) HST observations (Sromovsky *et al.* *Icarus* 149, 416–434, 459–488) provide new insights into the variations of Neptune and Triton over a variety of time scales. From 1996 WFPC2 imaging we find that a broad circumpolar nonaxisymmetric dark band dominates Neptune's lightcurve at 0.467 μm , while three discrete bright features dominate the lightcurve at longer wavelengths, with amplitudes of 0.5% at 0.467 μm and 22% at 0.89 μm , but of opposite phases. The 0.89- μm modulation in 1994, estimated at 39%, is close to the 50% modulation observed during the 1986 "outburst" documented by Hammel *et al.* (1992, *Icarus* 99, 363–367), suggesting that the unusual 1994 cloud morphology might also have been present in 1986. Lightcurve amplitudes in J–K bands, from August 1996 IRTF observations, are comparable to those observed in 1977 (D. P. Cruikshank 1978, *Astrophys. J. Lett.* 220, 57–59) but significantly larger than the 1981 amplitudes of M. J. S. Belton *et al.* (1981, *Icarus* 45, 263–273). The 1996 disk-integrated albedos of Neptune at H–K wavelengths are 2–7 times smaller than the 1977 values of U. Fink and S. Larson (1979, *Astrophys. J.* 233, 1021–1040), which can be explained with about 1/2–1/4 of the upper level cloud opacity being present in 1996. A simplified three-layer model of cloud structure applied to CCD wavelengths implies $\sim 7\%$ reflectivity at 1.3 bars (at $\lambda = 0.55 \mu\text{m}$,

decreasing as $\lambda^{-0.94}$) and $\sim 1\%$ at 100–150 mbars. To fit the WFPC2 observations and those of E. Karkoschka (1994, *Icarus* 111, 174–192), the putative H₂S cloud between 3.8 and 7–9 bars must have a strong decrease in reflectivity between 0.5 and 0.7 μm , as previously determined by K. H. Baines and W. H. Smith (1990, *Icarus* 85, 65–108). To match our 1996 IRTF results, this cloud must have another substantial drop in reflectivity at near-IR wavelengths, to a level of 0–5%, corresponding to single-scattering albedos of ~ 0 –0.3. The model that fits our near-IR observations on 13 August 1996 can reproduce the magnitudes of the dramatic 1976 "outburst" (R. R. Joyce *et al.* 1977, *Astrophys. J.* 214, 657–662) by increasing the upper cloud fraction to 6% (from $\sim 1\%$) and lowering its effective pressure to ~ 90 mbars (from 151 mbars). Triton's disk-integrated albedo from HST imagery at 11 wavelengths from 0.25 to 0.9 μm are consistent with previous groundbased and *Voyager* measurements, thus providing no evidence for the albedo decrease suggested by Triton's recent warming (J. L. Elliot *et al.* 1998 *Nature* 393, 765–767). Triton's lightcurve inferred from 1994–1996 WFPC2 observations has about twice the amplitude inferred from 1989 *Voyager* models for the UV to long visible range (J. Hillier *et al.* 1991, *J. Geophys. Res.* 96, 19,211–19,215). © 2001 Academic Press

Key Words: Neptune; Neptune, atmosphere; Triton; photometry.

1. INTRODUCTION

Multispectral Hubble Space Telescope (HST) imaging of Neptune in 1994, 1995, and 1996 provide a significant database of information concerning Neptune's atmospheric dynamics and vertical structure and its changes since the last detailed and extended view provided by the *Voyager* encounter in 1989. Wide Field Planetary Camera 2 (WFPC2) images that we obtained

¹ Based on observations made with the NASA/ESA Hubble Space Telescope, and on observations obtained from the data archive at the Space Telescope Science Institute. STScI is operated by the Association of Universities for Research in Astronomy, Inc. under NASA Contract NAS 5-26555.

² Visiting Astronomer at the Infrared Telescope Facility, which is operated by the University of Hawaii under contract to the National Aeronautics and Space Administration.

on 13–14 August 1996 are unique in their temporal coverage of a single rotation of Neptune and in their coordination with groundbased observations from the NASA Infrared Telescope Facility (IRTF). The observations and special data reduction procedures we developed to analyze 1996 and earlier observations are described by Sromovsky *et al.* (2001a), hereafter referred to as Paper I. Atmospheric circulation and spatially resolved cloud structure results obtained from these data are described by Sromovsky *et al.* (2001b), hereafter referred to as Paper III. The I/F values used to infer first-order vertical structure information in Paper III are based on the same photometric calibration discussed in this paper.

Here we describe the analysis that yields calibrated I/F values for the HST and IRTF data, and determine disk-integrated albedos of both Neptune and Triton at CCD and near-IR wavelengths. Neptune’s disk-integrated albedo and its rotational modulation are valuable in comparing with both recent observations, as well as observations dating back to 1972. The 1996 data provide a special insight into the relationship of disk-integrated properties to the spatial distribution of cloud features, which helps to interpret the long-term record of Neptune’s atmospheric dynamics. The disk-integrated spectrum of Triton and its rotational phase have value in tracking expected seasonal variations on Triton that cause migration of volatiles and resulting changes in Triton’s mean spectrum. By monitoring Triton’s spectral variations as a function of rotational phase we can place constraints on the distribution of surface ices. Triton’s disk-integrated absolute spectral lightcurve also has special value as a spectral reference for Neptune.

In the following sections we first provide a brief overview of the photometric methods applied to the HST image analysis, followed by a description of the IRTF photometric approach, with emphasis on aperture selection and seeing corrections. We next present the albedo and lightcurve results for Triton, the albedo and lightcurve results for Neptune, and finally, simplified models of Neptune’s cloud structure that are consistent with observed disk-integrated spectral properties and their short- and long-term

variations. In two appendices we discuss measurements of the IRTF point spread function (A) and standards of solar spectral irradiance (B).

2. HST PHOTOMETRY

We computed reflectivities for Neptune and Triton using

$$a(F) = \left(\frac{\text{DN}}{t_{\text{EXP}}} \right) \frac{\text{PHOTFLAM}(F)/\Omega}{(R_E/R_T)^2 E_{\odot}(F)/\pi}, \quad (1)$$

where DN is the WFPC2 digital number, t_{EXP} is exposure time, F denotes filter, R_E is the mean radius of the Earth’s orbit, R_T is the Sun–target distance at the time of the observation, $E_{\odot}(F)$ the average solar flux for each HST filter at a distance R_E and Ω denotes solid angles of either Neptune or Triton, for computation of disk-integrated albedos, or the solid angle of a single pixel, for computation of I/F values. Orbital distances, ranges, solid angles, and phase angles are provided in Table I. The geometric albedo, i.e., the disk-integrated albedo at zero phase angle, differs from our observed albedo by a small correction. Because the phase correction is not accurately known, we present the results here without correction (this is further discussed in regards to Triton’s lightcurve in Section 4.3).

In Eq. (1) the parameter PHOTFLAM is the point-source spectral flux density that produces 1 DN/s for a specific filter and A/D gain state, assuming a spectrally flat source and integration over an “infinite” aperture. The integral over the “infinite” aperture is operationally defined to be 1.096 times the flux contained within an aperture of 0.5” in radius (Voit 1997). For a spectrally varying source, the equivalent spectrally flat flux density is obtained by weighting the source spectrum with the HST system response functions. The WFPC2 filter characteristics, the current values of PHOTFLAM, and the average solar flux for each HST filter we used are provided in Table II. The standard deviation of the methane absorption coefficient within each filter bandpass is tabulated to demonstrate that there is too much variability

TABLE I
Observing Parameters for HST Observations

Date	Neptune–Sun distance (AU)	Range (AU)	Ω (Neptune) ^a (sr)	Phase angle ^b ([∘])	Ω (Triton) (sr)	Triton long. ^c ([∘])
10 Oct 1994	30.174	30.09	9.379E-11	1.89R	2.863E-13	160–140
18–19 Oct 1994	30.177	30.23	9.292E-11	1.89R	2.811E-13	27–(–6)
28 June 1994	30.177	29.20	9.956E-11	0.53L	3.012E-13	46–25
2 Nov 1994	30.173	30.47	9.141E-11	1.79R	2.765E-13	211–195
2 Sep 1995	30.169	29.46	9.781E-11	1.38R	2.959E-13	309–292
24 Nov 1995	30.166	30.77	8.964E-11	1.48R	2.709E-13	246–245
8 Mar 1996	30.164	30.78	8.958E-11	1.47L	2.710E-13	316–295
13 Aug 1996	30.161	29.24	9.929E-11	0.81R	3.004E-13	341–331

^a We used 1-bar values for Neptune’s equatorial and polar radii (Davies *et al.* 1992).

^b R(L) indicate that the Sun is right (left) of the central meridian (with N up).

^c The longitude scale for Triton is planetographic.

TABLE II
HST WFPC2 Filter Characteristics and Photometric Fluxes

Filter	$\langle \lambda \rangle^a$ (nm)	$\Delta \lambda^a$ (nm)	$\langle k(\text{CH}_4) \rangle^a$ (km-am) ⁻¹	$\sigma(k)^a$ (km-am) ⁻¹	PHOTFLAM ^b erg/(s cm ² Å)	$E_{\odot}(\text{F})^c$ W m ⁻² μm ⁻¹
F255W	260.59	45.02	0.0001	0.0000	5.736E-16	157.1
F336W	336.88	46.93	0.0048	0.0000	5.613E-17	871.5
F410M	409.42	18.61	0.0004	0.0000	1.031E-16	1682.2
F467M	467.09	20.89	0.0014	0.0005	5.763E-17	2015.4
F547M	548.77	63.79	0.0214	0.0032	7.691E-18	1856.7
F588N	589.36	6.54	0.0041	0.0021	6.125E-17	1776.2
F631N	630.64	4.21	0.0083	0.0064	9.148E-17	1661.3
F673N	673.22	6.33	0.0505	0.039	5.999E-17	1518.8
F850LP	912.47	106.91	5.68	1.02	8.357E-18	876.1
FQCH4N-B	621.82	4.49	0.624	0.49	9.059E-17	1708.1
FQCH4N-D	889.75	7.05	23.3	24.7	1.771E-16	921.8

^a $\Delta \lambda = \int S(\lambda) d\lambda$, $\langle \lambda \rangle = \int \lambda S(\lambda) d\lambda / \Delta \lambda$, $\langle k \rangle = \int k(\lambda) S(\lambda) d\lambda / \Delta \lambda$, $\sigma(k) = (\int (k(\lambda) - \langle k \rangle)^2 S(\lambda) d\lambda / \Delta \lambda)^{1/2}$, where $S(\lambda)$ is the filter-dependent relative response function versus wavelength, normalized to a unit maximum, and $k(\lambda)$ is the CH₄ absorption coefficient spectrum of Karkoschka (1994).

^b Values are for Gain = 7. Multiply by 10 to convert to W m⁻² μm⁻¹. Obtained from http://www.stsci.edu/instruments/wfpc2/Wfpc2_phot/wfpc2_photlam.html, last updated May 1997. The last two values were converted to gain = 7 using Table 28.1 of the HST Data Handbook (Voit 1997).

^c Average in-band solar irradiance at 1 AU = $\int S(\lambda) E_{\odot}(\lambda) d\lambda / \Delta \lambda$.

to accurately characterize the absorption by a single coefficient for each filter. Instead, we must compute radiation transfer at full resolution, or use exponential sums, and then integrate the results over the system response functions.

We treated Triton as a point source, using a circular aperture of 0.5'' in radius, with background values obtained from an annulus with inner and outer radii of 4'' and 6'' respectively. Our disk-integrated photometry of Neptune used an aperture diameter of 110 pixels (a radius of 2.5'') and a background annulus from 229 to 316 pixels in diameter, corresponding to a radial annulus from 5.2'' to 7.2''. From measurements of integrated count rates as a function of integration aperture size, we estimate that the infinite aperture value is 1% larger than our standard value, and have applied that correction prior to conversion to flux units. For long-exposure images, made at UV and methane-band wavelengths, numerous cosmic ray streaks are found throughout the images. These were removed from the planet disk by interpolation, using visual identification based on their characteristic morphology. They were also removed from the background sky using an automated technique that removes values exceeding a threshold level set to five standard deviations from the dark sky level, where the standard deviations are determined from small regions without cosmic ray hits.

3. IRTF PHOTOMETRIC ANALYSIS

3.1. Aperture Selection

Selection of an appropriate aperture for integration of energy from a given target is complicated by the extended wings of the point spread function (PSF), which make significant contributions. The approach we take is based on measured PSF profiles discussed in Appendix A.

Enclosed energy profiles and corrections. The enclosed energy as a function of aperture size varies significantly with seeing conditions (Fig. 1). Our procedure for dealing with these variations was to use a fixed aperture size for all seeing conditions, then apply seeing-dependent corrections to approximate the full integral. We used circular integration apertures and an annular region for background averaging that had approximately the same area as the integration aperture. The aperture size was chosen as large as possible within limitations of image frame size and avoidance of background contamination by other sources. We chose a central aperture diameter of $d_1 = 33$ pixels, which encloses 98% of the point-source energy when the seeing is 0.5'', and background annulus diameters of $d_2 = 43$ pixels and $d_3 = 56$ pixels. The seeing-dependent central and background integrals are used to estimate the seeing-independent infinite-aperture integral as described in the following.

Our operational measured aperture integral for point sources is given by the relation

$$S_M = S(d_1) - (S(d_3) - S(d_2)) \frac{d_1^2}{d_3^2 - d_2^2}, \quad (2)$$

where $S(d) = \int_0^{d/2} 2\pi r I(r) dr$ is the integral out to radius $r = d/2$. The second term of the equation is the background correction. Denoting $\beta(d) = S(d)/S(\infty)$, we can rewrite Eq. (2) in the form

$$S(\infty) = S_M \left[\beta(d_1) - (\beta(d_3) - \beta(d_2)) \frac{d_1^2}{d_3^2 - d_2^2} \right]^{-1} \quad (3)$$

The sizes of the corrections involved are summarized in Table III. The correction uncertainties are probably ~1% or

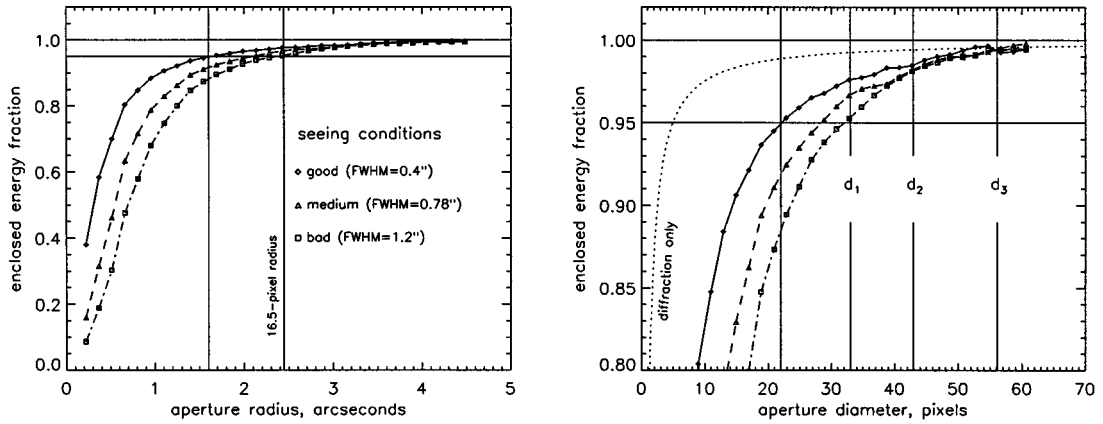


FIG. 1. Enclosed energy as a function of aperture radius (left) and a detailed view of the upper 20% as a function of aperture diameter in pixels (right). Our selected integration aperture is denoted by d_1 , while d_2 and d_3 indicate inner and outer annular diameters for background averaging. The diffraction curve is a theoretical calculation. The other curves are measurements of J-filter stellar images.

less, except that our estimate for $S(\infty)$ might be short by several percent, depending on how the wing behaves outside the radius range we investigated. However, that correction is probably the same for all seeing conditions, and because it applies as a factor that affects both reference star and target measurements, it cancels in the ratio. The primary role of our correction model is to accommodate changes in integral fractions between reference calibration measurements and target measurements, as might well occur because of changed seeing conditions. When we use a local reference for each image, such as Triton for doing Neptune photometry in the same image, correcting for missing energy is far less important.

Wavelength dependence of photometry corrections. The atmospheric seeing disk is only weakly dependent on wavelength, varying as $\lambda^{-0.2}$ (Walker 1987). Thus, over a wavelength range from 1.26 to 2.4 μm , this component would decrease by the factor $(1.26/2.4)^{0.2} = 0.88$, and the first-order effect would be correctly accounted for by the corrections given in Table III. More difficult to assess is the wing contribution, which presumably is a scattering effect and thus could depend rather strongly on wavelength. However, comparing measured K- and J-filter brightness profiles reveals no significant difference in either the core or the wing behavior. Perhaps this is accounted for by a size distribution in defects, such that different scales of particles or defects dominate at different wavelengths.

TABLE III
J-Filter Aperture Photometry Corrections

Seeing ^a	Seeing ^b	$\beta(d_1)$	$\beta(d_2)$	$\beta(d_3)$	$S(\infty)/S_M$
0.40''	0.47''	0.976	0.985	0.995	1.033
0.78''	0.88''	0.965	0.982	0.994	1.047
1.20''	1.23''	0.952	0.981	0.993	1.062

^a FWHM average over 7–9 images in each group.

^b Median FWHM of 2D Gauss fits within 17×17 box.

Aperture sizes and corrections for nonpoint sources. For objects of substantial angular extent, such as Neptune, and defocused star images, the aperture diameter needs to be increased by the diameter of the object in question, to ensure that energy from a limb point is collected with the same efficiency as that from a point source. We also modified the background integrals from that used for point sources so that annular radii would provide at least as much distance from the source but not get uncomfortably large. The aperture and annulus sizes are summarized in Table IV.

3.2. Photometric Calibration Methods

Our IRTF calibration is based on comparisons with standard stars observed at times and airmasses that are close to those used for our target measurements. Our starting point is the measured relative magnitude

$$\begin{aligned}
 m_r &\equiv -2.5 \cdot \log_{10} \left(\frac{\text{DN}}{t_{\text{EXP}}} \right) \\
 &= m(F, T, t) + m_E(F, T, t) - m_0(F, t)
 \end{aligned} \quad (4)$$

where $m(F, T, t)$ is the magnitude outside the atmosphere for filter F (J, H, K, etc.), for target T (star, Neptune, or Triton) at time t , and $m_E(F, T, t)$ is the corresponding atmospheric extinction. The photometric zero point $m_0(F, t)$ is the magnitude of a star that produces zero relative magnitude at zero air mass, following the sign convention used in the NSFCAM manual. The DN value may be for a single pixel, but more often is a sum over many pixels.

Magnitudes for Triton were obtained from segment averages closest to the air mass of the star observations, using a differential form of Eq. (4), namely

$$\begin{aligned}
 m(\text{Triton}) &= m(\text{star}) + [\bar{m}_r(\text{Triton}) - m_r(\text{star})] \\
 &\quad - k[\bar{X}(\text{Triton}) - X(\text{star})],
 \end{aligned} \quad (5)$$

TABLE IV
Summary of Aperture and Annular Diameters

Target object	Angular diameter	Pixel diameter	Target aperture d_1	Background annulus	
				d_2	d_3
In-focus star	0.0''	0	33	$33 \times 1.3 = 43$	$33 \times 1.7 = 56$
Triton	0.128''	0.9	33	43	56
Neptune	2.4''	16	$33 + 16 = 49$	$43 + 16 = 59$	$56 + 16 = 72$
Defocussed star	13.3''	85	$33 + 85 = 118$	$43 + 85 = 128$	$56 + 85 = 139$

in which we approximate $m_E(F, \text{Triton}) - m_E(F, \text{star})$ as the product of the air-mass difference [$\bar{X}(\text{Triton}) - X(\text{star})$] and the extinction per air-mass slope k . For observations made at nearly the same air mass as the stellar measurements, we used an analogous procedure to define Neptune's magnitude, except that a correction term δm was added to account for water vapor and CO₂ bands that produce differences in broadband extinction between Neptune and the reference sources. At a typical 1.4 air mass, we estimate that its J extinction was $\sim 7\%$ and $\sim 11\%$ less than reference sources on 13 and 14 August, respectively, and its K extinction was $\sim 7\%$ more on both nights. For H, Spencer 1.7, and CVF filters, δm was $\lesssim 1\%$. For other Neptune observations, we used Triton as a reference, first averaging its relative magnitude over segments of the observing period (typically ~ 0.5 h) to reduce noise, then using

$$m(\text{Nep}) = m(\text{Triton}) + [m_r(\text{Nep}) - \bar{m}_r(\text{Triton}) + \delta m] \quad (6)$$

to obtain the magnitude of Neptune within each segment. The advantage of using Triton as a reference is that it can be measured in the same image as Neptune, at the same time and with the same air mass, thus minimizing effects of extinction uncertainties.

We used two stars as magnitude references: faint star 34 on the UKIRT list, for calibrating broadband filter observations,

and a fairly bright star, γ Aql (HR 7525), for the narrowband filters. Their magnitudes are given in Table V. The air masses of our IRTF observations, listed in Table IV of Paper I, ranged from 1.3 to 2.36 for Neptune, 1.34–1.74 for UKIRT FS34, and 1.18–1.73 for γ Aql. Extinction slopes from 13 and 14 August 96 were not significantly different; by filter they ranged from 0.075 mag/air mass for the CVF 2.1- μm filter to 0.17 mag/air mass for the K filter. Given that most of our reference-to-target air-mass differences were 0.1 air masses or less, even our worst-case 0.05/magnitude uncertainty in extinction coefficient only yields a flux uncertainty of 0.005 mag, making this a negligible source of error.

To obtain γ Aql magnitudes for nonstandard filters (filters other than J, H, K) we first computed fluxes for a blackbody spectrum with an effective temperature of 4106 K and angular diameter of 7.5 ma, both from Dyck *et al.* (1998). Their ratios to the Vega fluxes provided an initial estimate of magnitudes. These agreed well with the K magnitude of Engels *et al.* (1981), but differed by 0.1 mag for the H magnitude. We thus adjusted the initial computed magnitudes by subtracting a wavelength-dependent offset of $0.154 \times (\lambda - 2.3 \mu\text{m})$, which produced a simultaneous match to Engels *et al.* (1981) measurements for both H and K filters. We increased uncertainties to 0.05 mag to roughly account for the additional uncertainty of the interpolation.

TABLE V
Reference Magnitudes and Fluxes for IRTF NSFCAM Filters

Filter	$\langle \lambda \rangle$ μm	$\Delta \lambda$ μm	UKIRT FS34 magnitude ^{a,c}	γ Aql magnitude ^{b,c}	Zero mag flux ^d $E_0(F)$ $10^{-9} \text{ W m}^{-2} \mu\text{m}^{-1}$	Solar flux ^e $E_\odot(F)$ $\text{W m}^{-2} \mu\text{m}^{-1}$
J	1.262	0.252	12.82 ± 0.014	0.33 ± 0.03	3.03 ± 0.09	443
H	1.633	0.269	12.92 ± 0.014	-0.36 ± 0.03	1.24 ± 0.04	238
Spencer H	1.740	0.097	12.93 ± 0.020	-0.41 ± 0.05	0.99 ± 0.03	195
K	2.199	0.390	12.99 ± 0.011	-0.54 ± 0.03	0.41 ± 0.01	86
CVF 1.59	1.590	0.032		-0.43 ± 0.05	1.21 ± 0.04	240
CVF 2.00	2.000	0.040		-0.49 ± 0.05	0.58 ± 0.02	116
CVF 2.07	2.070	0.041		-0.51 ± 0.05	0.51 ± 0.02	102
CVF 2.10	2.100	0.042		-0.52 ± 0.05	0.48 ± 0.02	98

^a Based on J–K, H–K, K, from Casali and Hawarden (1992).

^b J, H, K from Engels *et al.* (1981).

^c Other values are computed as described in the text.

^d Computed from Kurucz model matched to Brown *et al.* (1985).

^e Computed solar flux at Earth's mean distance (see text for basis).

TABLE VI
Triton Magnitudes on 13, 14 Aug 1996

Filter	13 Aug 1996	14 Aug 1996	Difference (14–13)
J open	12.20 ± 0.02	12.12 ± 0.02	−0.08 ± 0.03
H	12.08 ± 0.02	12.06 ± 0.02	−0.02 ± 0.03
Sp 1.7	12.01 ± 0.03	11.99 ± 0.03	−0.02 ± 0.04
K	12.24 ± 0.02	12.29 ± 0.03	+0.05 ± 0.03
CVF 1.59	11.99 ± 0.06		
CVF 2.00	12.27 ± 0.06		
CVF 2.07	12.24 ± 0.09		
CVF 2.10	12.29 ± 0.08		

Note. UKIRT FS34 is the reference for J, H, Sp, 1.7, K. γ Aql. is the reference for CVF filters. JHK airmass differences: 0.05 on 13 and 14 Aug. CVF airmass difference: 0.10.

Zero magnitude fluxes for all filters were computed from the model Vega spectrum of Kurucz (personal communication, 1998) scaled by 2.653×10^{-16} to match the Brown *et al.* (1985) 1.4–2.6 μm Vega spectrum, which is itself based on measurements by Blackwell *et al.* (1983). The fluxes were computed using the referenced spectrum and IRTF filter functions in Eq. (7). Our zero-magnitude fluxes for J, H, and K filters are respectively 0.914, 1.075, and 0.993 times those computed by Cohen *et al.* (1992) for the corresponding UKIRT filters. Our quoted uncertainties are based on the uncertainties in the Brown *et al.* (1985) spectrum.

Our derived Triton magnitudes are summarized in Table VI. The uncertainties are derived from scatter in the measured relative magnitudes and uncertainties in the stellar reference sources. No magnitudes are given for CVF filters on 14 August because of stellar contamination. These results were obtained at Triton orbital planetographic central meridian longitudes of 336° – 337° on 13 August and 274° – 275° on 14 August, and at a phase angle of 0.81° . Small corrections may be required to obtain mean magnitudes at zero phase (see Section 4).

3.3. Conversion of Magnitudes to Fluxes and I/F

Our magnitude scale is defined in terms of the average spectral flux density within each filter passband, i.e.,

$$\begin{aligned} \bar{E}(T, F, t) &\equiv \frac{\int S(F, \lambda) E(T, \lambda, t) d\lambda}{\int S(F, \lambda) d\lambda} \\ &\equiv E_0(F) 10^{-m(F, t)/2.5}, \end{aligned} \quad (7)$$

where $S(F, \lambda)$ is the IRTF-NSFCAM total instrument response function for filter F and $E(T, \lambda, t)$ is the spectral irradiance of target T at wavelength λ and time t , referenced to the top of the atmosphere, and where $E_0(F)$ is the average flux at zero magnitude (using instrumental spectral weighting), and $m(F, t)$ is the magnitude of the target, as determined directly or indirectly from stellar comparisons using Eqs. (5) and (6). NSFCAM filter response functions are given in Paper I. Filter characteristics and zero magnitude fluxes are listed in Table V.

We computed the reflectivity, or I/F values, using the expression

$$a(F, T, t) = \frac{\pi R_T^2 E_0(F)}{\Omega R_E^2 E_\odot(F)} \times 10^{-m(F, t)/2.5}, \quad (8)$$

where Ω is the solid angle of the target, R_T is its distance from the Sun, R_E is the mean orbital radius of the earth, and $E_\odot(F)$ is the spectral irradiance of the Sun averaged over the instrumental response function for filter F . These solar flux averages are listed in Table V. When the solid angle Ω includes the entire planetary disk, this becomes the disk-integrated albedo. When applied to measurements at zero phase angle, this becomes the geometric albedo.

In computing the average solar fluxes for each filter, we used a composite solar irradiance reference described in Appendix B. Because of significant errors in the commonly used Arvesen *et al.* (1969) spectrum, we used the model spectrum of Kurucz (1994) for the region 1–2.5 μm , an approach also taken by Colina *et al.* (1996).

4. ALBEDO AND LIGHT CURVE OF TRITON

In addition to their value in establishing a photometric reference for Neptune, Triton's geometric albedo spectrum and lightcurve have direct scientific value of their own. As Triton's southern hemisphere approaches summer solstice (~ 2000 AD), large changes in frost distribution are expected (Yelle *et al.* 1995) and thus monitoring Triton's infrared spectral behavior during the coming decade should provide useful insights into the dynamics of surface ices on Triton (Brown *et al.* 1995). From occultation observations in 1995 and 1997, Elliot *et al.* (1998) concluded that Triton's atmosphere has undergone a global warming with the resultant doubling of atmospheric bulk every 10 years. According to Model F of Spencer and Moore (1992), this result is consistent with a frost albedo decrease by 0.12 between 1989 and 1997. However, our results suggest that little change has occurred in Triton's mean albedo since 1989–1990, although there does seem to be a change in Triton's lightcurve.

4.1. Triton's Albedo at CCD Wavelengths

The Triton HST disk-integrated albedo results for 13 August 1996 and 18 October 1994 are summarized in Table VII and compared in Fig. 2 with 1989 *Voyager* imaging results (Hillier *et al.* 1990). *Voyager* photopolarimeter results (Nelson *et al.* 1990), an IUE measurement at 0.27 μm (Stern *et al.* 1989), and 1990 groundbased results (Buratti *et al.* 1994). The Stern *et al.* result was corrected to a Triton radius of 1352 km. For filters common to both 1994 and 1996 HST data sets it can be seen that 1996 albedos are about 4% higher than 1994 values. This might be due to the difference in phase angles. The 1994 results are for a phase angle of 1.89° , while the 1996 data were obtained at a phase angle of 0.81° . If we use the phase coefficient of Gougen *et al.* (1989) we would expect 1996 albedos to be

TABLE VII
HST WFPC2 Determinations of Triton's Disk-Integrated Albedo

Triton long.:	123°–159°	6–27°	195°	292°–309°	300°–362°
Phase angle:	1.89°	1.89°	1.79°	1.38°	0.81°
Filter\date:	10, 11 Oct 94	18 Oct 94	2 Nov 94	2 Sep 95	13, 14 Aug 96
F255W					0.43 ± 0.04
F336W		0.62 ± 0.04			0.65 ± 0.05
F410M		0.71 ± 0.04			0.74 ± 0.04
F467M	0.71 ± 0.03	0.72 ± 0.03	0.73 ± 0.03	0.73 ± 0.03	0.73 ± 0.03
F547M	0.723 ± 0.015	0.743 ± 0.015	0.771 ± 0.015	0.743 ± 0.015	
F588N					0.772 ± 0.016
F631N					0.844 ± 0.017
F673N					0.794 ± 0.016
F850LP					0.826 ± 0.017
FQCH4N-B		0.761 ± 0.015			0.792 ± 0.016
FQCH4N-D		0.684 ± 0.014			0.713 ± 0.015

Note. Triton's central meridian longitude is planetographic.

$2.7 \pm 3.8\%$ higher, compared to the observed 3–4%. Another possible contribution could be a difference in Triton longitudes coupled with a longitude-dependent albedo. The longitude difference noted in Table VII is not large enough, nor is Triton's lightcurve well enough defined, to make a good case for this as the primary cause, although it cannot be ruled out (see Section 4.3 for further discussion of Triton's lightcurve). The Buratti *et al.* (1994) observations in 1990 were made on 19 June, with a phase angle of 0.6° and a Triton planetographic longitude $\sim 80^\circ$ – 140° . In comparison with the 1996 HST results, the Buratti data need no phase correction, but might be expected to be somewhat lower because the longitudes sampled have been and may still be somewhat darker (see Section 4.3). However, the Buratti results are in excellent agreement with the HST results.

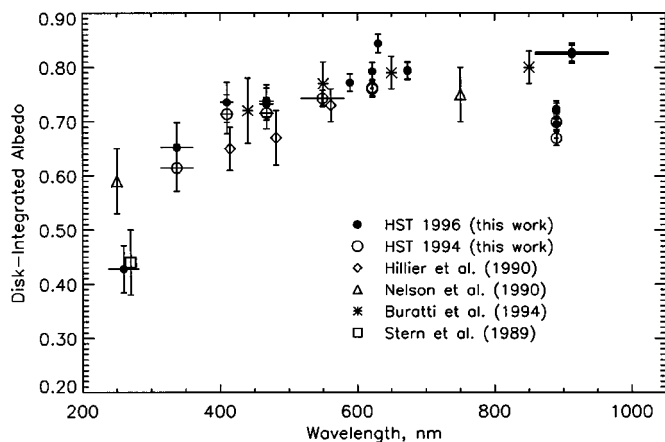


FIG. 2. Disk-integrated albedo of Triton based on 1996 and 1994 HST observations, in comparison with *Voyager* results (diamonds) by Hillier *et al.* (1990) using the ISS and (triangles) by Nelson *et al.* (1990) at 0.25 and 0.75 μm using the photopolarimeter, with an IUE result (squares) at 0.27 μm (Stern *et al.* 1989), and with 1990 groundbased results (asterisks) by Buratti *et al.* (1994). See text for phase angles and Triton orbital phase. September 1995 results at 467 and 547 nm (listed in Table VII) would overlap the 1994 results if included in this plot. For the HST points, horizontal bars indicate filter bandwidths.

Errors in our HST results are dominated by three components: uncertainty in the HST calibration, uncertainty in the solar irradiance spectrum, and measurement noise. The HST calibration is generally accurate to about 2% RMS or better for standard photometric filters and broad and intermediate filters in the visible and better than 5% RMS for narrowband filters in the visible (Voit 1997). The uncertainty in the solar irradiance spectrum is hard to estimate accurately. Differences between Neckel and Labs (1984) and Arvesen *et al.* (1969) are relatively flat, with Arvesen a few percent higher, but differences are up to 10% at 330–340 nm, 7–10% at 380–395 nm, and 7% at 410–420 nm. These differences are quite a bit larger than the 1–2% uncertainties estimated by the authors. Recent space-based measurements by Woods *et al.* (1996) have estimated errors of 5–7% accuracy in the spectral range 330–400 nm, with even larger uncertainties at shorter wavelengths. Comparisons between Woods *et al.* (1996) and other measurements in this spectral range seem compatible with these estimates. Thus we have assigned somewhat conservative approximate uncertainties of 2% to the solar irradiance spectrum for wavelengths beyond 500 nm, 4% at 467 nm, 5% at 410 nm, 7% at 336 nm, and 7% at 255 nm. Measurement noise of the Triton aperture integrals contributes a relatively small noise that reaches a maximum of 0.7% at 410 nm.

Discussion: An albedo feature at 890 nm? Both the 1994 and 1996 HST observations using the methane quad filters seem inconsistent with other measurements. This is especially clear for 1996, where we find that the F850LP result is consistent with the lack of a significant wavelength dependence in the region 0.6–1 μm , while the FQCH4N-D result suggests a significant drop of 12–13% at 890 nm. This is possibly a consequence of the vignetting of the methane quad filters, which causes the greatest perturbations at the edge of the image, where Triton is located when Neptune is close to the center of the image. On the other hand, the low albedo near 890 nm could be partly a real effect. In the summer of 1989, Grundy and Fink (1991) measured a relative depression of $6.0 \pm 0.6\%$ at 890 nm, which they

attribute to absorption by CH₄ ice. Had no change occurred since 1989, this might explain half of our observed depression. Also, given observed global warming on Triton since 1989 (Elliot *et al.* 1998), the albedo depression at 0.89 μm might easily have increased. However, Sromovsky *et al.* (1998) presented a relative grism spectrum of Triton that closely matched that of Cruikshank *et al.* (1993) in the depths of CH₄ absorption features between 2 and 2.4 μm providing evidence against significant change between 1991 and 1998. Our CVF and broadband filter measurements at these wavelengths in 1996 (discussed in the following section) are also compatible with no change between 1991 and 1996, although these observations are not as sensitive to the methane absorption features. The weight of the evidence suggests that at least half of the 890-nm albedo depression we observed in 1996 is probably an artifact.

4.2. Triton's Albedo at near-IR Wavelengths

Our disk-integrated albedo results of Triton (Table VIII) were obtained by inserting the magnitudes from Table VI into Eq. (8). The tabulated uncertainties are derived from magnitude uncertainties and uncertainties in the solar flux integrals. As noted previously, there was background contamination by a nearby star on 14 August that prevented meaningful CVF filter measurements of Triton on that day.

The wavelength dependence of Triton's disk-integrated albedo is displayed in Fig. 3, where our discrete filter results are seen to agree closely with 1992 spectra obtained by Cruikshank *et al.* (1993). The broadband results for 13 and 14 August also agree within estimated errors, except for J-filter, where a larger difference might be an indication of a small rotational modulation (the longitude difference is 62°). These results provide little evidence for changes in the mix or distribution of surface ices on Triton since the 1991–1992 period of Cruikshank's observations. Historical evidence for variations in this part of the spectrum are discussed by Brown *et al.* (1995). There is some evidence that the 1.65- μm absorption feature (due to CH₄ ice) was significantly weaker in 1981, and that the 2.34- μm feature (also primarily due to CH₄ ice) was stronger in 1986. However,

TABLE VIII

Triton's Disk-Integrated Albedo on 13, 14 Aug 1996

Filter	13 Aug 1996	14 Aug 1996	Difference
J open	0.85 ± 0.05	0.92 ± 0.03	+0.07 ± 0.04
H	0.73 ± 0.02	0.74 ± 0.02	+0.02 ± 0.03
Sp 1.7	0.75 ± 0.03	0.77 ± 0.03	+0.02 ± 0.04
K	0.58 ± 0.02	0.56 ± 0.02	-0.03 ± 0.02
CVF 1.59	0.77 ± 0.05		
CVF 2.00	0.59 ± 0.04		
CVF 2.07	0.61 ± 0.05		
CVF 2.10	0.57 ± 0.04		

Note. References: UKIRT FS34 for J-K, γ Aql for CVF. JHK airmass differences: 0.05, 0.10 on 13, 14 Aug. CVF airmass difference: 0.10 on 13 Aug.

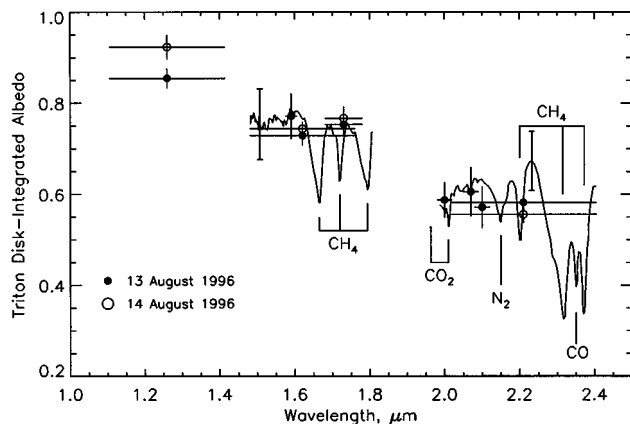


FIG. 3. Disk-integrated albedo of Triton as a function of wavelength, comparing average IRTF results from 13–14 August 1996 (Table VIII) with spectra from Cruikshank *et al.* (1993). The error bars for the Cruikshank spectra are from Brown *et al.* (1995). Spectral features are due to absorption by surface ices of N₂, CH₄, CO, and CO₂. Horizontal bars indicate spectral ranges of the filters; vertical bars indicate uncertainties.

both of those changes are probably too small to resolve with our 1996 observations.

4.3. Triton's Lightcurve

Definition of Triton's lightcurve has scientific value because it places constraints on the changing distribution of ices over Triton's surface. Understanding variations related to orbital phase is required to distinguish those from longer-term seasonal variations due to migration of volatiles. It also has value in making use of Triton as a photometric reference for Neptune observations. The rotational lightcurve amplitude for Triton is expected to be quite small; e.g., Lark *et al.* (1989) found no more than a 2% variation at 8900 Å, while Hillier *et al.* (1991) found about 4% (peak-to-peak) in the visible range (based on *Voyager* observations). These are relatively small variations, comparable to the absolute calibration uncertainty in the HST observations. However, in lightcurve measurement it is relative errors that matter most, and these are much smaller than the absolute errors. Baggett and Gonzaga (1998) showed that fluctuations of photometric throughput for filters F336W and longward are ±1% or less over 4 years.

The exceptional photometric stability of the WFPC2 and the lack of any need to determine variable extinction corrections that complicate groundbased measurements provide significant advantages in the measurement of lightcurves. However, there is one complication that arises when the object is not at a fixed location in the image frame: variations in charge-transfer efficiency (CTE) with image coordinates. The CTE effect causes faint stars to appear typically 4% brighter near the bottom of the image frame (high line numbers) than they do at the top of the frame (Holtzman *et al.* 1995). Because Neptune is approximately centered in our HST data sets, Triton circles around the outer part of the image frame, producing a varying line number that correlates with Triton's orbital phase, thus creating an automatic

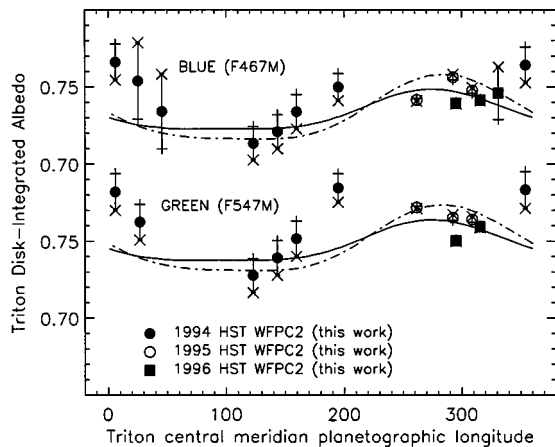


FIG. 4. Triton's lightcurve at 467 and 547 nm, according to 1994–1996 HST observations, compared to Hillier *et al.* (1991) relative models for 350 nm (dot-dash) and 560 nm (solid) based on *Voyager* observations. Models have been scaled to provide an approximate match to HST absolute values. HST values have been corrected for CTE effects (Whitmore *et al.* 1999) and corrected to their average phase angle of 1.45° using $\beta = 0.025$. The upper (+) and lower (\times) phase correction limits are based on Gougen *et al.* (1989). The sign of the correction is positive when the observed phase is larger than the average phase, and negative otherwise.

correlation between CTE effects and Triton's central meridian longitude. If no CTE correction is made, a false lightcurve of several percent modulation is implied for an object as bright as Triton. To approximately remove this effect we used correction equations provided by Whitmore *et al.* (1999). Because Triton is so far from the center of the image frame we also need to apply a photometric correction for distortion effects, as given by Fig. 5.12 in the *WFPC2 Instrument Handbook* (STScI 1996). This correction typically decreases the integrated DN by 1.5%.

In Fig. 4 our 1994–1996 HST estimates of Triton's lightcurve from F467M and F547M filter observations are compared to *Voyager*-based synthetic lightcurves by Hillier *et al.* (1991). Because the HST observations are taken over a variety of phase angles, we have corrected the observations to the average phase angle of 1.45° using the Gougen *et al.* (1989) phase coefficient of 0.025 ± 0.035 . Phase correction uncertainties are shown as vertical bars terminating with \times and $+$ to indicate the corrections respectively resulting from the lower and upper limits of the phase coefficient. For a given observation, the sign of the correction depends on whether the phase angle is smaller or larger than the mean phase.

Our lightcurve results agree with Hillier *et al.* (1991) that Triton is darker near 100° planetographic longitude and are crudely consistent with their brightness maximum near 280° , but do not agree with the details of either their observed (not shown) or model curves. (It should be noted that Hillier *et al.*, and most previous observers in this field, expressed results in terms of a longitude = $360^\circ -$ planetographic longitude.) We find a peak-to-peak amplitudes of 5.6% (0.06 mag) for F467M (blue) and of 7.8% (0.08 mag) for F547M (green), which are about twice what Hillier *et al.* obtained at 560 nm. The synthetic

curves were developed for a subobserver latitude of 50° S, to approximate *Voyager* observing conditions. The sub-Earth latitude in 1994 was 48.1° S, very close to the model value. Thus the variation in lightcurve amplitude with the changing sub-Earth latitude does not explain the discrepancy between the model lightcurve and the points we derived from HST observations.

To obtain a reasonable degree of orbital phase coverage, we had to combine results from three different observing years, which might raise questions about drifts in the photometry as partly responsible for lightcurve disagreements. The photometric stability results of Bagget and Gonzaga (1998) can be further strengthened by comparing Triton's variation in time with that of Neptune's. According to Lockwood and Thompson (1991), Neptune's variation over an entire solar cycle is only about 4% at these wavelengths, so that only a small variation might be expected over the 1994–1996 period. From the HST observations we find that Neptune's disk-integrated variation is only about 1% over this period, well below the nearly 8% observed for Triton. From this comparison it is clear that Triton's variation is not an artifact. There remains the possibility that changes in Triton's lightcurve from year to year have produced some distortions in the derived lightcurve. However, the most robust result, the steep slope in the 120 – 180° longitude range, is all from a single year.

According to models of Hillier *et al.* (1991), Triton's lightcurve amplitude should decrease as $1/\lambda$, at least up to 890 nm, where it should equal about 2%. Unfortunately, there are very few reliable HST observations that can be used to confirm this. The F850LP observations in 1996 do not cover a long enough time period by themselves, and the 1994–1995 observations used only the methane quad filters, which have considerable vignetting in the region of the image where Triton is usually located.

The closely spaced HST observations in Fig. 4 give consistent indications of brightness variations with longitude, with slopes comparable to those measured by Hillier *et al.* (1991), but not at the same longitudes. Because the *Voyager* results had to be corrected for widely varying phase angles, while the HST observations are all at very small phase angles, it is probable that the HST observations provide a more accurate description than the Hillier *et al.* predictions of the 1994–1996 lightcurve. Analysis of additional wavelengths, especially longer wavelengths for which Triton's rotational lightcurve has a small amplitude, and shorter wavelengths for which the amplitude should be greatest, may yield better constraints on the lightcurve.

5. ALBEDO AND LIGHTCURVE OF NEPTUNE

5.1. Neptune's Rotational Lightcurve at WFPC2 Wavelengths

An accurate description of Neptune's lightcurve on 13 August 1996 can be obtained at CCD wavelengths from our HST observations with WFPC2, which provide almost complete coverage of one rotation for F467M, F673N, and F850LP filters, and a good sampling at several other wavelengths. Our direct measurements are displayed in Fig. 5, from which we estimate

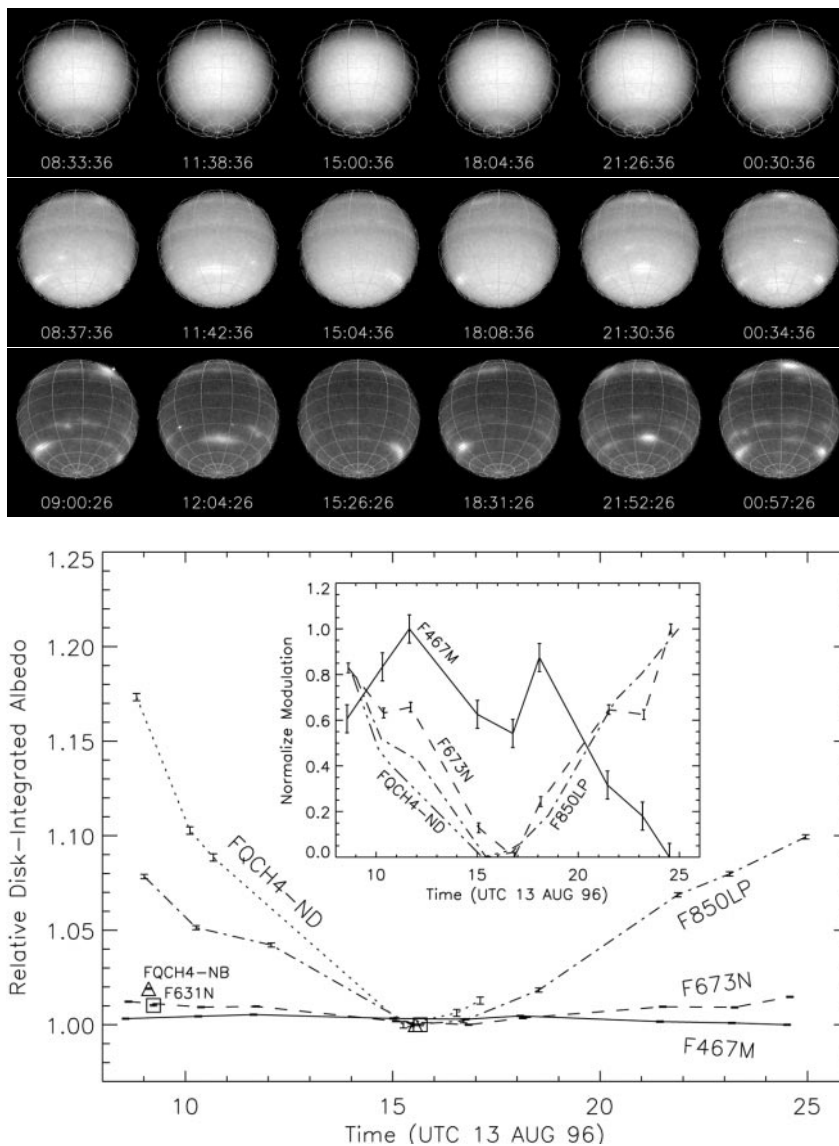


FIG. 5. Neptune's lightcurve during one rotation on 13 August 1996, as obtained from HST disk integrations scaled to a unit minimum. Error bars indicate statistical uncertainties in disk integration. Systematic errors during one rotation are probably less than 0.2%. The inset curve displays the shape of the modulation by plotting differences from the minimum divided by the maximum difference for each filter. Cloud features in view during the rotation are indicated by the sequence of images in the upper panel. The 467M curve is dominated by dark features, the rest by bright features.

peak-to-peak amplitudes of $0.5 \pm 0.1\%$ for F467M, $1.7 \pm 0.1\%$ for F673N, $10.0 \pm 0.3\%$ for F850LP, and $22 \pm 1\%$ for FQCH4-ND. Our value at $0.89 \mu\text{m}$ is equivalent to 0.22 mag, which is comparable to the 1986 value obtained by Hammel *et al.* (1989), but about half of their 1987 value. However, relatively large modulation amplitudes can be found in the 1994 HST data. On 10 October 1994, opposite sides of Neptune differed by 39% (0.36 mag) at $0.89 \mu\text{m}$, which is close to the 1987 value of 0.44 mag of Hammel *et al.* (1992), and thus is a possible indication of what Cruikshank (1985) and Hammel *et al.* (1992) referred to as an "outburst." This is further discussed in Section 5.5 and in Paper III.

The main features of the 1996 lightcurves are understandable from a comparison with the time sequence of images in the upper panel of Fig. 5. There are three prominent bright clouds that have significant influence on the lightcurve, two near 45°S and one near 40°N , the latter being the companion to the dark spot at 35°N . In methane-band filters they are seen with great contrast, but at 673N the contrast is much reduced, and at 467M it is essentially absent. For F850LP (and FQCH4-ND, the $0.89\text{-}\mu\text{m}$ filter), the lightcurve maximum is achieved when three bright clouds are visible on the disk, and the minimum when only one is visible. This is also true for the 673N filter (and for FQCH4-NB, the $0.62\text{-}\mu\text{m}$ filter), except that the lightcurve amplitude is

reduced by the smaller feature contrast and the shape is slightly different because these two bands are relatively more sensitive to the southern clouds and less sensitive to the northern companion cloud.

It is interesting to note that the F467M lightcurve reaches a minimum where other curves reach a maximum. The 467M images show that this filter does not have any significant response at all to the bright cloud features. Instead, it is the filter that is most sensitive to dark features. Although the transit of two dark spots contributes to the variation, it is relatively small because the features are of low contrast and heavily limb darkened. The primary variations seen in the 467M lightcurve arise from varying views of the dark band surrounding the southern pole. As described in detail in Paper III, that band is a wavenumber-one feature at an average latitude of 60°S , and a latitudinal amplitude of $\sim 5^\circ$, resulting in a 10° north–south wobble as the planet rotates. When its northern-most excursion is in view, the dark fraction of the Earth-facing disk is increased and the disk-integrated albedo is thereby decreased. When the band is seen at its southern most excursion, the dark fraction is at a minimum, raising the disk-integrated albedo. The influence of dark features on Neptune’s lightcurve provides possible explanations of some puzzling aspects of past groundbased observations, as noted in the following discussion.

Comparisons with previous observations. Neptune’s disk-integrated albedo has been known for some time to vary with rotational phase. Belton *et al.* (1981) used the variations in the shape of the K–J lightcurve during July and August 1980 to infer that there were several cloud features present with different rotational periods, suggesting that Neptune’s winds varied with latitude. Hammel *et al.* (1989) used CCD imaging to show that lightcurves at methane-band wavelengths in 1996 and 1997 were each dominated by a single bright cloud feature. They obtained lightcurve amplitudes at $0.89\ \mu\text{m}$ of about 0.2 mag in 1986 and 0.5 mag in 1987, but less than about 0.05 mag at continuum wavelengths of 0.826, 0.749, and $0.634\ \mu\text{m}$. In the methane bands, the high contrast between discrete bright cloud features and the dark background atmosphere is seen to yield larger amplitude lightcurves. At shorter wavelengths, constraints on lightcurve amplitudes can be obtained from Lockwood and Thompson’s long-term tracking of Neptune’s brightness with b ($0.472\ \mu\text{m}$) and y ($0.551\ \mu\text{m}$) filters (Lockwood and Thompson 1991, Lockwood *et al.* 1991). Standard deviations of these observations, reported by Hammel *et al.* (1992), remained below 0.004 mag (0.4%) from 1972–1985, but increased to 0.0085 (b) and 0.0095 (y) in 1987. The b and y standard deviations in 1987 correspond to lightcurve amplitudes of 2.4 and 2.7% respectively, assuming a randomly sampled sinusoidal lightcurve, for which the standard deviation is just the peak-to-peak fractional amplitude divided by $2\sqrt{2}$. On the other hand, if we consider the standard deviation of 0.4% as measurement noise, then the implied lightcurve amplitudes would be 2.1 and 2.4%. In either case, these are much larger than the 0.5% amplitude that we found for the F467M filter in 1996.

Discussion: The possibility of major dark features in 1987. Hammel *et al.* (1992) present the interesting result that the b and y standard deviation peaks in 1987 are reached a year after the peak in the $0.89\text{-}\mu\text{m}$ lightcurve amplitude, and that during the $0.89\text{-}\mu\text{m}$ peak the b standard deviation was near its normal value of 0.004 mag. It is clear that the shortwave filters were not seeing merely attenuated versions of what is seen in the methane band. Our 1996 observations, showing that dark features can play an important role at short wavelengths, suggest the possibility that these disk-integrated observations with b and y filters are providing information about dark features that might have been present following the peak in the bright cloud features. It is conceivable that the 1989 GDS appeared between the time of the 1986 and 1987 observations, and that it would be well positioned in the southern hemisphere to have a maximal impact in the disk-averaged albedo observed from the Earth. However, in 1989 the GDS represented only about 4–6% of the total cross-sectional area when on the central meridian, and thus, assuming the *Voyager* blue contrast value of $\sim 10\%$ for this feature (Smith *et al.* 1989), it should contribute only about 0.4–0.6% to the peak-to-peak lightcurve amplitude, about 1/4 the value inferred from the b -filter observations in 1986. Perhaps the GDS was larger in 1987, or the second dark spot was much larger, or other nonaxisymmetric dark features, such as the south circumpolar wave, were more prominent then.

5.2. The Disk-Integrated Albedo of Neptune at WFPC2 Wavelengths

The disk-integrated albedo results from the 1994 and 1996 WFPC2 observations are presented in Table IX and Fig. 6. The 1994 results were obtained from seven successive images between 15:00 UT and 17:02 UT on 18 October (data sets u23j0401–407). The 1996 results were obtained from 18 images

TABLE IX
HST Determinations of Neptune’s Disk-Integrated Albedo

Filter	$\langle \text{HST} \rangle$		1996 lightcurve ^a correction factors	Groundbased ^{b,c} 23–26 July 1993
	18 Oct 1994	13 Aug 1996		
F255W		0.52 ± 0.04		
F336W	0.54 ± 0.04	0.55 ± 0.04		0.563
F410M	0.57 ± 0.03	0.58 ± 0.03		0.574
F467M	0.55 ± 0.02	0.56 ± 0.02	0.998	0.575
F547M	0.42 ± 0.01			0.454
F588N		0.440 ± 0.009		0.471
F631N		0.365 ± 0.007		0.379
F673N		0.215 ± 0.004	0.997	0.233
F850LP		0.043 ± 0.001	0.992	0.044
FQCH4N-B	0.113 ± 0.003	0.114 ± 0.002		0.119
FQCH4N-D	0.0195 ± 0.0004	0.018 ± 0.001	0.987	0.0226

^a Factor to correct for rotational sampling (not applied).

^b The Karkoschka (1994) spectrum weighted with HST filter functions.

^c Uncertainties are 2% relative, 4% absolute.

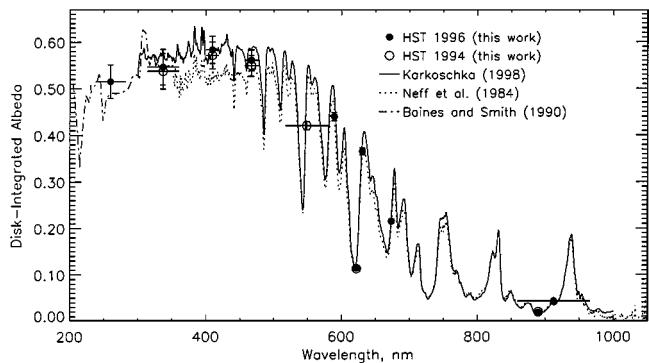


FIG. 6. Disk-integrated albedo of Neptune based on 13 August 1996 and 18 October 1994 HST observations, in comparison with groundbased results by Neff *et al.* (1984) (dotted line) and Karkoschka (1994) (solid curve). The Neff results were increased by 3% to account for changes in adopted values of Neptune’s radii. Filter bandpasses are shown as horizontal lines. The fine-structure for $\lambda < 400$ nm is due to Raman scattering.

from 8:33 UT to 12:16 UT on 13 August (data sets u3fc0101-10; in Table II of Paper I). We used the measured lightcurve for 1996 to determine correction factors that would convert the 1996 averages to averages over a complete lightcurve. The corrections, listed in Table IX, are below 1% for most filters, and only 1.3% for the FQCH4N-D filter. Although we have no corresponding lightcurve measurement to assess the representativeness of the 1994 observations, from the visual appearance of images during our averaging periods, in comparison to those at other times, we estimate that the means for 1994 are probably within 1% of true rotational means, with the possible exception of the FQCH4N-D value, which might deviate by 1–2%. Examination of the 1994 images we used shows that more bright clouds than those in the 1996 images were present at low latitudes. (These unusual low-latitude features, known as the “bright complex,” are discussed in Paper III.) This might explain why the FQCH4N-D albedo for 1994 is $\sim 10\%$ larger than the value for 1996. The other albedo values for corresponding filters in 1994 and 1996 are insignificantly different.

The HST albedo values for 1994 and 1996 (Fig. 6) compare reasonably well with groundbased results for 1993 and 1995 Karkoschka (1994, 1998) and for Neff *et al.* (1984). The latter have been increased by 3.4% to correct them to the current 1 bar radii of Neptune (Davies *et al.* 1992). According to Karkoschka (1998) the major reason for the difference between his spectrum and that of Neff *et al.* is the use of different values for the solar irradiance spectrum. Karkoschka uses a solar analog spectrum that we believe to be in good agreement with the Neckel and Labs (1984) spectrum that we used for the range 330 to 869 nm. The two Karkoschka spectra for Neptune show no significant change between 1993 and 1995, except possibly for deep methane-band wavelengths beyond about $0.85 \mu\text{m}$. At $0.89 \mu\text{m}$ the ratio of the two spectra (1995/1993) is about 0.95. Given the 17.5% lightcurve amplitude we observed in 1995, and the even larger amplitude that was present in 1994, it is cer-

tainly possible that the difference in the two Karkoschka spectra could be due to observing different average phases of Neptune’s lightcurve.

For a more precise comparison with Karkoschka’s spectrum we computed average albedos for each of the HST filters, weighting the albedo spectrum by the product of the solar irradiance and the HST system response function for each filter. The results (Table IX) show that difference between the HST and ground-based averages over the same bandpasses are generally inside the error bars, although the groundbased results average 4% higher, including all filters but FQCH4N-D. For that filter (at $0.89 \mu\text{m}$) Karkoschka’s albedo is 29% larger than our 1996 albedo, and 15% larger than our 1994 value. These differences probably mean that the fractional coverage of bright discrete cloud features was somewhat greater during the 1993 and 1995 observing periods. While significant albedo changes on Neptune have occurred even at shorter wavelengths ($\sim 4\%$ at 472 and 551 nm), these occur on times scales comparable to the solar cycle (Lockwood and Thompson 1991), and thus would not be expected to contribute much over a 2-year period. A more likely explanation for the 4% difference over the other filter bands is a systematic calibration difference, which is in fact the same size as the absolute error quoted by Karkoschka.

5.3. Comparison of the 0.3–1.0 μm Spectrum with Model Calculations

Using the same temperature and mixing ratio profiles, and the same methane and CIA absorption computational methods as described in Paper III, we computed Neptune’s geometric albedo for a clear atmosphere containing a thin high-altitude haze, and for models with additional tropospheric reflecting layers. We computed multiple scattering using the doubling and adding methods of Hansen and Travis (1974), and accounted for Raman scattering effects using the model derived by Karkoschka (1994, 1998). The aim of these calculations is to provide insight into the way tropospheric scatterers can influence Neptune’s spectrum, and thus what the measured spectrum implies about the vertical location of such scattering aerosols and their relative contributions to Neptune’s I/F spectrum.

If its atmosphere were purely Rayleigh scattering and conservative, Neptune’s geometric albedo would be about 0.75 (Bergstrahl and Baines 1984), far above its measured maximum near 0.6 (Karkoschka 1994). Even after methane absorption and Raman scattering are taken into account, an additional high-altitude absorbing haze is needed to explain the measured albedo at shorter wavelengths. Using haze optical depths comparable to those of Pryor *et al.* (1992) we obtained the “cloud-free” model displayed in the upper part of Fig. 7. This model captures most of the gross features of Neptune’s spectrum, but has two significant discrepancies: the peaks and valleys of the weak methane bands ($0.45\text{--}0.60 \mu\text{m}$) are both too low and the stronger methane bands ($0.6\text{--}1 \mu\text{m}$) are deeper and broader than observed. Scattering by upper tropospheric aerosols must be added to achieve reasonable agreement with the measurements.

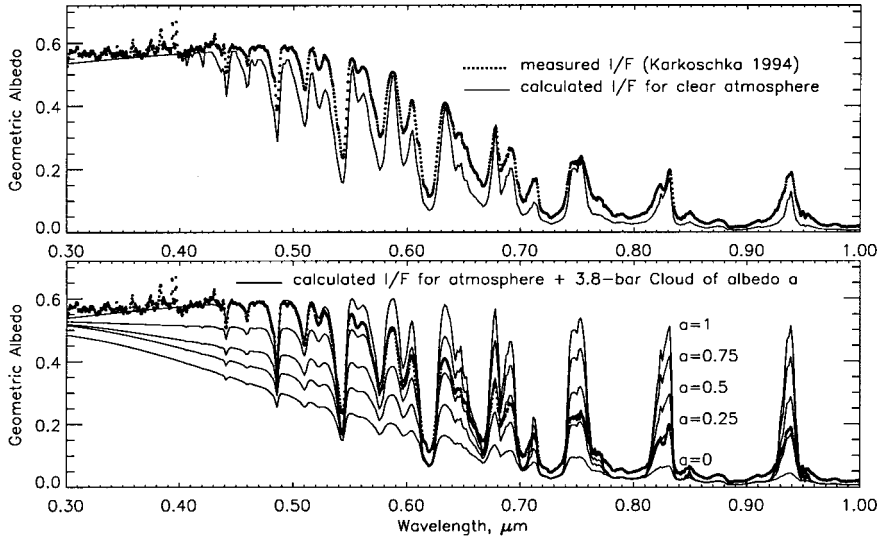


FIG. 7. (Top) Comparison of Neptune’s measured geometric albedo (Karkoschka 1994) with a “cloud-free” model calculation, showing the need for increased scattering in deep methane bands and at $0.5\text{--}0.6\ \mu\text{m}$. (Bottom) Comparison of measurements with model calculations including a 3.8-bar reflector at equal albedo increments, showing approximate linearity and the need for reduced lower cloud albedo for $\lambda > 0.6\ \mu\text{m}$.

Because there is so little methane above the tropopause (100–400 mbars), scattering layers in that region have a particularly strong influence on Neptune’s spectrum at wavelengths beyond $0.5\ \mu\text{m}$. Only about 1% coverage of high-albedo upper tropospheric clouds is needed to fill in the deep methane bands at 0.8, 0.89, and $1\ \mu\text{m}$, but that amount of cloud has a negligible influence at short wavelengths. A much larger fractional contribution is required to fill in the deficit in the range $0.45\text{--}0.6\ \mu\text{m}$. This region can be well fitted by a reflecting layer near 3.8 bars, the nominal revised fit to the bottom cloud top pressure by Baines *et al.* (1995). This layer is plausibly composed of H_2S aerosols extending down to the H_2S condensation level near 7 bars. Model calculations for such a layer are illustrated in the lower half of Fig. 7, for layer albedos from 0 to 1 in increments of 0.25. With a high albedo this layer can produce the needed boost at $0.45\text{--}0.6\ \mu\text{m}$, but, as noted by Baines and Smith (1990) and Baines and Hammel (1994), this cloud cannot be as highly reflective at longer wavelengths because it would be in violent disagreement with the low continuum I/F values measured beyond $0.6\ \mu\text{m}$. Beyond $0.8\ \mu\text{m}$, the albedo of that layer must be no more than ~ 0.25 . Figure 7 also shows that for $\lambda > 0.5\ \mu\text{m}$ there is a roughly linear relationship between the lower cloud albedo and the geometric albedo of Neptune. We later take advantage of this special linear relationship in simplifying model fits to the spectrum. This does not apply at short wavelengths where multiple reflections between the atmosphere and the 3.8-bar reflector create the nonlinearity that generally characterizes multiple scattering.

Even if the single-scattering albedo of this cloud is reduced as needed to be compatible with the peak I/F values in this region (near 0.75 , 0.83 , and $0.935\ \mu\text{m}$), it produces peak shapes that are too narrow. That problem is nicely handled by adding a second tropospheric layer of scatterers near the 1.3-bar level,

which can be plausibly associated with condensed methane particles. Multiple-scattering calculations including a thin 1.3-bar cloud with optical depths from 0 to 0.1 also show an approximate linear relationship between I/F and optical depth of this cloud, a characteristic we will also take advantage of in fitting model calculations to observations. From imaging observations it is clear that much of the upper-level scattering that dominates methane-band wavelengths arises from discrete features rather than from a horizontally homogeneous layer. We do not know what opacity range is valid for these highest clouds, but if they consists of opaque elements, then their I/F contributions will be a linear function of their effective fractional coverage amounts.

The above considerations lead to a three-layer upper tropospheric model consisting of a homogeneous reflecting layer at 3.8 bars with a spectrally varying albedo, a homogeneous transparent cloud near 1.3 bars, as needed to improve the shape of the deeper methane bands, and a heterogeneous reflecting layer at 100 mbars to represent the effects of clouds that are above most of the methane. We take advantage of the computational convenience of the approximate linear relationships previously noted and use a linear combination of layer contributions to model Neptune’s disk-averaged I/F spectrum as

$$I = f_{\text{haze}}[f_{0.1}I_{0.1,1} + f_{1.3}I_{1.3,1} + (1 - f_{0.1} - f_{1.3})[a_{3.8}I_{3.8,1} + (1 - a_{3.8})I_{3.8,0}]] \quad (9)$$

$$a_{3.8} = \frac{a_{\text{min}} + a_{\text{max}} \exp(-(\lambda - \lambda_0)/\delta\lambda)}{1 + \exp(-(\lambda - \lambda_0)/\delta\lambda)}, \quad (10)$$

where f_{haze} is a multiplier that adjusts the effective stratospheric haze absorption that was included in the calculation of $I_{0.1,1}$, $I_{1.3,1}$, and $I_{3.8,1}$, which are the disk-integrated I/F spectra that

would result from unit albedo homogeneous lambertian reflectors placed at 0.1, 1.3, and 3.8 bars respectively. $I_{3.8,0}$ is the corresponding spectrum for a zero albedo surface at 3.8 bars. The fractional coverage amounts for the upper two layers, as seen from above the atmosphere, are given by $f_{0.1}$ and $f_{1.3}$. We chose to parameterize both middle and upper layers in terms of a fractional coverage (as seen from above the clouds) of unit albedo reflectors at the pressures indicated by subscripts. From multiple-scattering experiments we find that an effective fraction $f_{1.3}$ corresponds to an optical depth of $\tau_{1.3} \approx 2.2f_{1.3}$, assuming unit albedo particles with the Pryor *et al.* phase functions. These I/F calculations include the multiple-scattering Rayleigh atmosphere, Raman scattering, and haze extinction using a wavelength-dependent function $\tau_h = 0.05(\lambda/0.75 \mu\text{m})^{-0.78}$ that we matched to Pryor *et al.* (1992). Although this linear combination approach is not strictly valid at short wavelengths, the nonlinearities that exist there are really unimportant for two fortuitous reasons: (1) to fit the observations, the deep 3.8-bar cloud must have essentially unit albedo for which we do not really need to interpolate, and (2) the small coverage fractions (or optical depths) of the upper and middle clouds contribute so little at short wavelengths that errors in computing their contributions at these wavelengths are unimportant. The virtue of this approach is that it allows a small set of very time-consuming multiple-scattering calculations to be used to accurately fit the observed I/F spectrum with iterative nonlinear regression techniques.

To accommodate an equivalent variation of opacity with wavelength, we included a wavelength dependence in the fractional coverage of the 1.3-bar cloud as $f_{1.3}(\lambda) = f_{1.3,0.55} \times (\lambda/0.55 \mu\text{m})^{n_{1.3}}$, which might be expected for particles not much larger than the wavelengths considered. In modeling the wavelength dependence of the albedo of the lower cloud, we assume that $a_{\text{max}} = 1$, as suggested by the shortwave behavior of the Baines and Hammel (1994) results. The remaining parameters allow for adjustment of the transition wavelength, λ_0 , the transition width $\delta\lambda$, and the minimum albedo a_{min} that is the limiting value at long wavelengths.

From nonlinear χ^2 minimization we found best-fit parameters values of $f_{\text{haze}} = 1.055 \pm 0.04$, $f_{0.1} = 0.0114 \pm 0.0004$, $f_{1.3,0.55} = 0.072 \pm 0.003$, $n_{1.3} = -0.94 \pm 0.12$, $a_{\text{min}} = 0.24 \pm 0.01$, $\lambda_0 = 0.611 \pm 0.001 \mu\text{m}$, $\delta\lambda = 0.051 \pm 0.002 \mu\text{m}$, where the errors quoted are the combined random uncertainties obtained from the χ^2 analysis and the 4% absolute calibration uncertainty quoted by Karkoschka (1994). The 1.3-bar fraction evaluates to 0.05 at $0.75 \mu\text{m}$, which scales to an equivalent optical depth of 0.11. This is much higher than the global average optical depth of 0.03 inferred by Baines and Smith (1990) at the same wavelength, but between the values 0.05 and 0.34 Baines and Hammel (1994) found for equatorial and 22°S – 30°S regions, respectively. Our fit of the 3.8-bar albedo parameters confirms that the 3.8-bar scattering layer has a greatly reduced albedo beyond $0.5 \mu\text{m}$ as shown in the bottom panel of Fig. 8. This is equivalent to a strong decrease in the single-scattering albedo of particulates in this layer, to ~ 0.8 at $0.9 \mu\text{m}$, in approximate agreement with Baines and Smith (1990) and Baines

and Hammel (1994). This is not a physically appealing solution because the obvious candidate cloud materials (H_2S or NH_3) do not have the proper red-absorbing characteristic, as evident from frost spectra of Lebofsky and Fegley (1976). Nevertheless, the model spectrum, shown as the heavy solid curve in Fig. 8, does an excellent job of fitting the observations. At most wavelengths, the fit is comparable to the 2% relative error in the measurements (Karkoschka 1994). While the fit is close and the parameters are well constrained by the observations, this does not rule out the possibility that alternative models might be constructed that fit as well.

The haze correction factor amounts to a decrease in the haze extinction optical depth by about 0.02 relative to the assumed Pryor *et al.* (1992) values of 0.19 ± 0.08 at $0.265 \mu\text{m}$ and 0.05 ± 0.02 at $0.75 \mu\text{m}$. The adjustment is within their error bars.

The effective fractional amount of high-altitude cloud that is needed to fill in the deep methane bands to the level of the Karkoschka (1994) measurements is extremely small ($f_{0.1} \approx 1\%$), while rather large changes in cloudiness at deeper levels have little impact at $0.89 \mu\text{m}$ because of the strong absorption by the overlying CH_4 . Because the fraction of Neptune's disk that contains bright cloud features generally exceeds 1% (see Fig. 5, for example), the upper clouds must be heterogenous at a subpixel level, as is suggested by many of the high-resolution *Voyager* images (Smith *et al.* 1989), or the clouds must be partly transparent.

5.4. Neptune's Disk-Integrated Albedo at near-IR Wavelengths

The time dependence of Neptune's near-IR disk-averaged albedo from NSFCAM images on 13 and 14 August 1996 is displayed in Fig. 9. Each plotted value is an average over several images to reduce noise levels, with averaging time segments indicated by horizontal bars. The cause for the albedo decrease during the 13 August observing period is the bright cloud near 30°N , which rotated out of view as the evening progressed. This is illustrated by the J-filter images in Fig. 10 and the HST image sequence in Fig. 5. In Fig. 9 we also show the lightcurve obtained from the WFPC2 F850LP filter, scaled and offset to provide a best match to the near-IR values for three representative filters. The shape of the very time-limited IR variation on 13 August is well matched by these fits. From this comparison we conclude that the peak-to-peak differences seen in the IRTF images are roughly half of the full lightcurve modulation for most filters.

The directly measured maximum to minimum albedo differences are 18% (0.18 mag) for J, 31% (0.30 mag) for H, 92% (0.71 mag) for Spencer 1.7, and 181% (1.12 mag) for K. Using the fitted WFPC2 shape function, we estimate peak-to-peak values for the complete lightcurves to be 55% (0.47 mag) for J, 72% (0.59 mag) for H, 126% (0.88 mag) for Spencer 1.7, and 269% (1.42 mag) for K. The percentage differences are computed as $100 \times (\text{max}/\text{min} - 1)$, and magnitude differences as $2.5 \log_{10}(\text{max}/\text{min})$. Our estimated J–K amplitude is then about 0.95 mag for 13 August 1996, which is in close agreement with the 1.09 mag obtained for 12–13 July 1977 by Cruikshank (1978), even though he obtained a surprisingly small

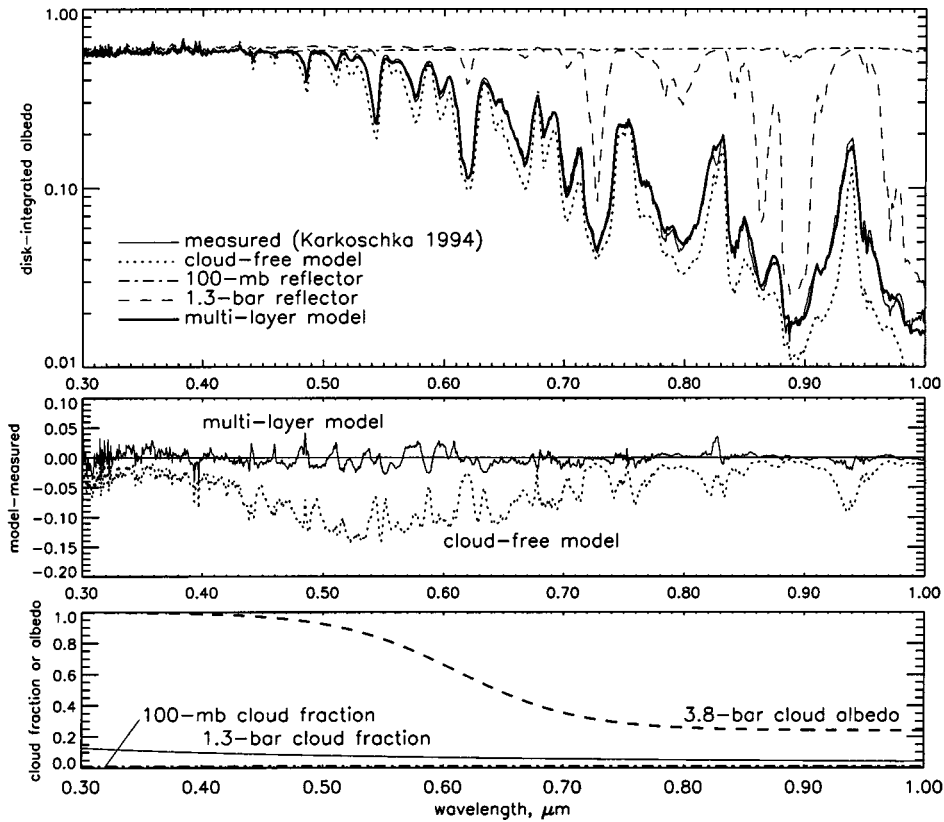


FIG. 8. (Top) Model computations of Neptune’s geometric albedo (thick solid curve) compared to groundbased results (thin solid curve) by Karkoschka (1994). All models include stratospheric absorbing haze. (Middle) Small differences between model and measured albedo spectra demonstrate the excellent fit obtained by the simple multilayer model. (Bottom) The variation of wavelength-dependent model parameters shows that the putative H₂S cloud seen at 3.8 μm must become very dark for $\lambda > 0.6 \mu\text{m}$.

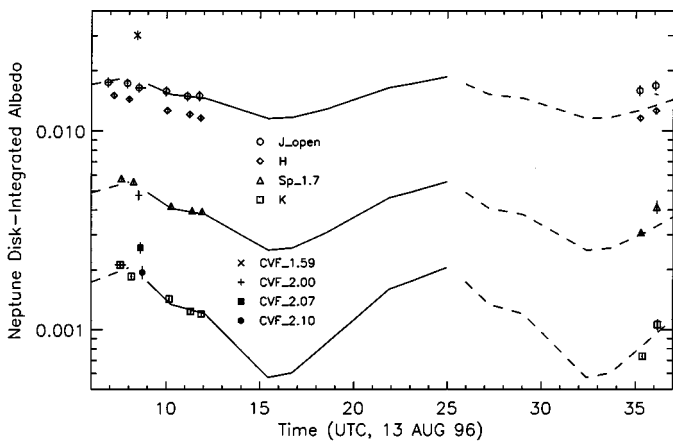


FIG. 9. Disk-integrated albedo of Neptune derived from 13–14 August IRTF NSFCAM images. Horizontal bars indicate averaging periods, vertical bars indicate albedo uncertainties. The solid curves are offset and scaled versions of the HST-derived lightcurve obtained for the F850LP filter, given in Fig. 5. The dashed curves are estimated lightcurves, obtained by offsetting the solid curves by 17 h, which is the average rotation period of the bright features that dominate the lightcurves.

K-magnitude variation (0.85). Belton *et al.* (1981) obtained only about 0.5 mag for J–K modulation during July and August 1981. While these 1977 and 1981 values are roughly comparable to what we observed in 1996, it is likely that much larger IR modulations would have been obtained in 1986, when the 0.89- μm modulation (Hammel *et al.* 1989) was four times larger than we observed in 1996. Presuming the difference is caused by the larger fractional coverage of bright clouds near the tropopause, a factor of 4 increase would also have been expected for the IR lightcurve amplitudes during 1986.

The wavelength dependence of Neptune’s near-IR disk-integrated albedo is displayed in Fig. 11, where our discrete filter averages for 13 and 14 August 1996 (Table X) are compared to the 1977 spectrum of Fink and Larson (1979). Given the large effect of discrete cloud features on the albedo in this spectral range, we should not expect close agreement between these two sets of measurements. An overall calibration problem in our results is unlikely because the same calibration is used to obtain our Triton albedos, which are in reasonably close agreement with previous results. The most plausible explanation is that Neptune’s bright cloud features were more prominent in 1977 than in 1996. This interpretation is further explored with model calculations that are described in the next section.

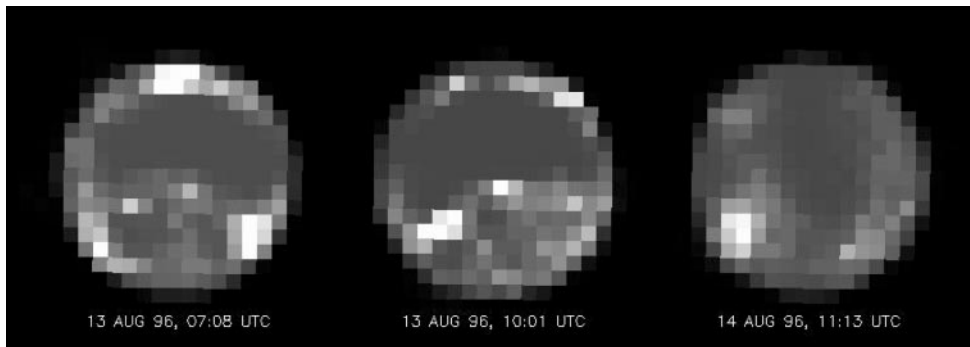


FIG. 10. J-filter images of Neptune illustrating discrete cloud characteristic for the IRTF data sets used to determine disk-integrated albedos for 1996. The first two characterize conditions on 13 August, and the third characterizes conditions on 14 August.

5.5. Comparison of the 1–2.5 μm Spectrum with Model Calculations

Following the same procedures described in Paper III, we calculated model spectra in the range 1–2.5 μm for the three-layer model of tropospheric scattering developed to fit the 0.3–1 μm spectrum. In this model, the disk-integrated albedo is represented as a linear combination of geometric albedos of reflecting layers at specific pressure levels, i.e.,

$$I = f_{p_{\text{hi}}} I_{p_{\text{hi},1}} + f_{1.3} I_{1.3,1} + (1 - f_{p_{\text{hi}}} - f_{1.3}) [a_{3.8} I_{3.8,1} + (1 - a_{3.8}) I_{3.8,0}], \quad (11)$$

where $I_{p_{\text{hi},1}}$, $I_{1.3,1}$, and $I_{3.8,1}$ are the disk-integrated I/F values that would be valid for horizontally homogeneous unit albedo reflecting layers at high, middle, and low altitudes respectively

(at pressures p_{hi} , 1.3 bars, and 3.8 bars), and $I_{3.8,0}$ is the corresponding spectrum for a zero albedo surface at 3.8 bars. The f value for each level represents fractional cloud amounts (for heterogeneous opaque layers) or fractional reflectivity (for semi-transparent layers), and $a_{3.8}$ is the albedo of the reflecting layer at 3.8 bars. This model follows the same form as Eqs. (9), (10), except that the extinction optical depth of stratospheric haze is taken to be 0.02 less than the fit to the Pryor *et al.* (1992) values. This representation of geometric albedo as a linear combination is valid for upper and middle clouds that are either opaque (and heterogeneous) or of such low opacity that multiple reflections between layers do not need to be accounted for. In this spectral range the atmospheric Rayleigh scattering contribution is well approximated by single scattering (see Paper III).

In formulating a model that could reproduce the essential features of Neptune's near-IR spectrum, we first tried to

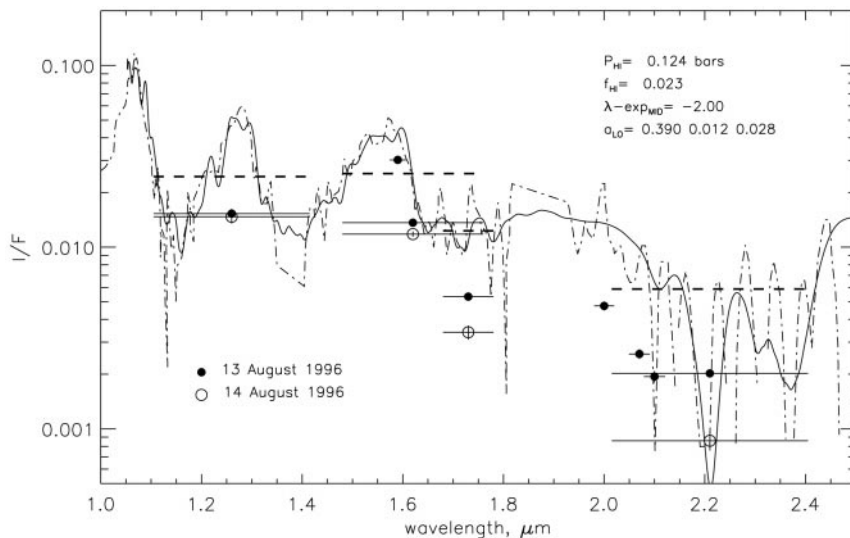


FIG. 11. Disk-integrated albedo of Neptune as a function of wavelength, comparing average results from 13–14 August 1996 IRTF observations (Table VIII) with 1977 measurements (dash-dot curve) of Fink and Larson (1979), and a model fitted (solid curve) to the Fink and Larson spectrum (see text for model description). Horizontal bars indicate spectral ranges of the filters; vertical bars indicate uncertainties. The modulations in the Fink and Larson spectrum in the range 2.1–2.4 μm are at the noise level. The dashed segments are averages of the model fitted to the Fink and Larson spectrum, weighted by filter and solar irradiance functions.

TABLE X
Average Disk-Integrated Albedo of Neptune by Filter

Filter	13 Aug 1996		14 Aug 1996		1977 model	Outburst model
	Measured	Model	Measured	Model		
J open	0.0153 ± 0.0009	0.0159	0.0147 ± 0.0009	0.0138	0.024	0.046
H	0.0136 ± 0.0004	0.0141	0.0118 ± 0.0004	0.0118	0.025	0.047
Sp 1.7	0.0053 ± 0.0002	0.0050	0.0034 ± 0.0003	0.003	0.012	0.030
K	0.0019 ± 0.0001	0.0018	0.0008 ± 0.0001	0.0010	0.006	0.020
CVF 1.59	0.0302 ± 0.0016	0.0260				
CVF 2.00	0.0047 ± 0.0003	0.0050				
CVF 2.07	0.0026 ± 0.0002	0.0031				
CVF 2.10	0.0019 ± 0.0001	0.0020				

extrapolate the model developed to fit the CCD spectral observations. We initially used $a_{3.8} = 0.024$ (the asymptotic value for long wavelengths) and $f_{1.3} = 0.041(\lambda/1 \mu\text{m})^{-0.94}$, which is our previous middle cloud wavelength dependence function referenced to $1 \mu\text{m}$ instead of $0.55 \mu\text{m}$. We then separately computed each term of Eq. (11) and compared them (Fig. 12) to the observed spectrum of Fink and Larson (1979). It is apparent that the upper cloud contribution is constrained by the I/F values in the strong CH_4 and H_2 bands where it is the dominant contributor. The CCD model has only about one-half the upper cloud amount needed to match the Fink and Larson spectrum, which is not at all surprising, given the variability of the high-altitude discrete features on Neptune. The relative spectral variations within these strong absorption bands is compatible with clouds at ~ 120 mbars. The extrapolated 1.3-bar contribution is also reasonably compatible with the Fink and Larson spectrum, in the sense that it does not exceed the measurements, even when added to the 120-mbars contribution.

The main problem with the extrapolation arises from the 3.8-bar contribution. While it is compatible with the measured peak

at $1.07 \mu\text{m}$, it alone greatly exceeds the measured I/F in the other window regions near 1.27 and $1.58 \mu\text{m}$. To accommodate a cloud at 3.8 bars, the observations require that the cloud have a greatly reduced albedo within these windows, although the precise albedo values are not well constrained. When we add the 1.3-bar I/F contribution to the 120-mbar contribution, there is little room for any additional I/F from the 3.8-bar cloud layer, unless we reduce the overall fractional contribution of the 1.3-bar cloud, or increase its wavelength dependence, both of which are conceivable differences that might have occurred between times of CCD and near-IR spectral observations. More significantly, the spectral details are not sufficiently well resolved by the observations to permit a clear distinction between these middle and low cloud contributions at near-IR wavelengths. Thus we are forced to be somewhat arbitrary in how we partition these two contributions.

We chose to use for our nominal model a mid-level fraction of $f_{1.3} = 0.041(\lambda/1 \mu\text{m})^{-2}$, which agrees with the CCD model at $1 \mu\text{m}$, but has a stronger wavelength dependence that leads to slightly better fits and less pathological albedos for the 3.8-bar

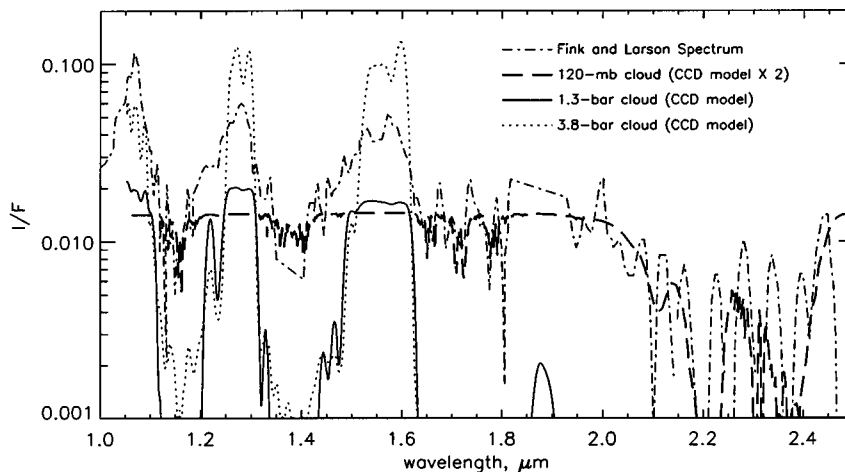


FIG. 12. Disk-integrated albedo of Neptune as a function of wavelength, comparing model components derived from fitting Karkoschka's 1994 spectrum, with 1977 measurements (dash-dot curve) of Fink and Larson (1979). The 3.8-bar cloud component is a major contributor to the peak at $1.07 \mu\text{m}$, but is incompatible with observations in the longer wavelength windows, unless its albedo is substantially reduced in those windows.

TABLE XI
Reflecting Layer Combination Fits to near-IR
Observations of Neptune

Parameters	Model for Fink and Larson	Model for 13 Aug 96	Model for 14 Aug 96	Model for 1976 outburst
p_{hi} , bars	0.124 ± 0.010	0.151 ± 0.015	0.151	0.089
f_{hi}	0.023 ± 0.001	0.009 ± 0.001	0.005	0.057
$f_{(1.3,1\mu)}$	0.041	0.010 ± 0.008	0.010	0.010
$a_{(3.8,1\mu)}$	0.387	0.387	0.387	0.387
$a_{(3.8,1.27\mu)}$	0.012	0.060	0.060	0.060
$a_{(3.8,1.6\mu)}$	0.028	0.028	0.028	0.028

cloud. We chose three parameters to describe the 3.8-bar cloud, $a_{(3.8,1)}$, $a_{(3.8,1.27)}$, and $a_{(3.8,1.6)}$, the albedos at 1, 1.27, and 1.6 μm . Linear interpolation is used between these values, and a constant is assumed for $\lambda > 1.6 \mu\text{m}$. Besides the three albedo values, the fitting algorithm also adjusted the pressure of the upper cloud, p_{hi} , and its fractional coverage, f_{hi} , for a total of 5 adjustable parameters.

The best fit to the Fink and Larson spectrum is shown in Fig. 11, with averages over the IRTF bandpass filters listed in Table X. The best-fit parameter values and uncertainties (for those that are tightly constrained) are listed in Table XI. The weighted averages over the fitted spectra for each filter are shown by heavy dashed lines extending over each filter bandpass. The solid curve is the best-fit spectrum, smoothed to provide better compatibility with the measurements. Note, however, that the model is unable to reproduce well the detailed spectral features of the continuum peaks. Better spectral resolution and signal/noise in the observations would be valuable in refining future models. The most reliable aspect of the current model fit is the inference concerning upper cloud characteristics because

they are almost entirely constrained by the behavior in the strong absorption bands, where radiation cannot reach the lower layers.

In fitting the 13 August 1996 bandpass-filter observations, we assumed the same lower cloud albedos as found from fitting the Fink and Larson spectrum, except that we found it necessary to increase the combined reflectivity contributing to the 1.27- μm window, which we chose to obtain by adjusting the lower cloud albedo at this wavelength. While retaining the previously assumed wavelength dependence for the middle cloud, we were unable to obtain a reasonable fit unless we adjusted the overall middle cloud fraction. The fit results for 13 August observations are presented in Fig. 13 and Tables X and XI. As before, the solid curve is the best-fit spectrum. The weighted averages over the fitted spectra for each filter are shown by heavy dotted bars. While the upper level cloud top pressure retrieved from the 13 August 1996 observations is similar to that needed to fit the Fink and Larson (1979) spectrum, the retrieved fractional cloud amounts for upper and middle cloud layers both appear to be reduced by at least a factor of 2.

The 14 August 96 observations are less complete due to star interference, and thus do not provide enough constraints to warrant a full independent fit of all parameters. However, it is easy to approximately match the 14 August results by adjusting just the fractional coverage of the upper cloud (Table XI). This is the only parameter that provides the across-the-board I/F reduction in the 1.7- and 2.3- μm absorption bands. A spectrum with the upper cloud fraction reduced to 0.0048, shown as the dot-dash curve in Fig. 13, has about the right characteristics needed to match the 14 August observations. The bandpass filter averages for this spectrum are also listed in Table X.

The reduced upper cloud amount of the 14 August model is at least roughly consistent with the reduction in the number of bright discrete cloud features visible (Fig. 10). Although it has a

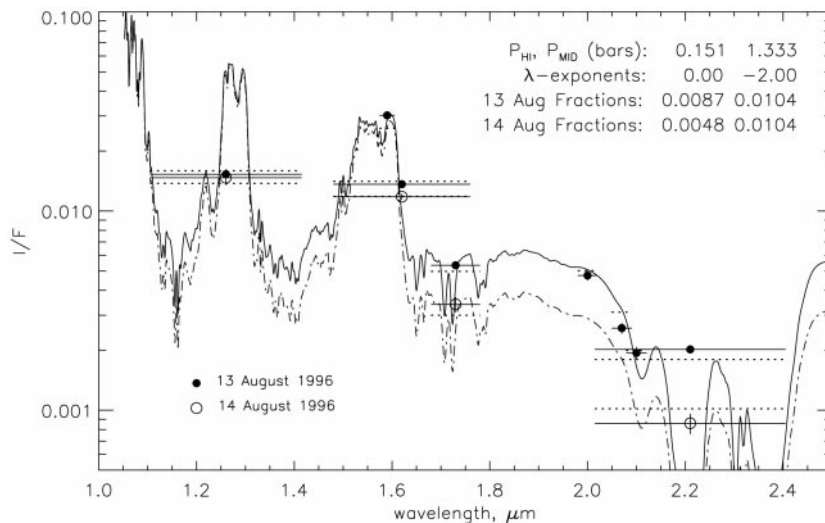


FIG. 13. Model fits to 1996 measurements of Neptune's disk-integrated near-IR albedo. Parameters for the solid-line spectrum are given in the figure. The bandpass filter-weighted I/F averages over this spectrum are indicated by dotted line segments spanning the filter bandpass. The dot-dash spectrum has half the upper level cloud fraction, and a cloud level pressure of 50 mbar.

very small fractional coverage this upper level cloud is dominant at wavelengths of strong methane absorption. Whether there is a small additional scattering contribution by an ubiquitous high-altitude haze is not determined from these observations, but localized I/F observations in the equatorial region (see Paper III) have found very little evidence of an upper level (100 mbars or so) haze contribution.

The model fits discussed above were disk-integrated models based on essentially 1-dimensional models of vertical structure, and do not account for the fact that the upper level cloud contribution is dominated by a small number of discrete features at specific view angles. Models that do account for this are treated in Paper III.

Discussion: Albedo characteristics of 3.8-bar cloud particles. Our modeling results for the putative H_2S cloud have been expressed in terms of the normal albedo of a reflecting layer at 3.8 bars. To make more direct comparisons of our results with previously derived single-scattering albedos for the cloud particles, it is necessary to establish a relationship between that parameter and cloud reflectivity that our models constrain. For that purpose we carried out multiple-scattering calculations for a semi-infinite layer of isotropic particles and for particles with phase functions matching those derived by Pryor *et al.* (1992), both as a function of single-scattering albedo of the cloud particles. We then used those results to convert our cloud reflectivity values to equivalent single-scattering albedos. The combined results from CCD and near-IR fits are displayed in Fig. 14, along with previous determinations at CCD wavelengths by Baines and Smith (1990) and Baines and Hammel (1994). At most wave-

lengths our values are somewhat lower when converted using the isotropic phase function results (solid line) rather than the Pryor *et al.* (1992) phase function (dotted line).

At CCD wavelengths, our results are in reasonably close agreement with previous estimates, especially in the amplitude of change over the CCD range and in the maximum slope of the transition between high and low albedo. The main difference is in the wavelength of the transition, which we find to be $\sim 0.03 \mu\text{m}$ longer than previous estimates. This difference might be a result of our fitting to the Karkoschka (1994) spectrum, which has a larger maximum and falls off more slowly than the Neff *et al.* (1984) spectrum used by earlier modelers. Our use of a lambertian reflecting model might also have contributed to this difference. Our multiple scattering calculations show that limb darkening is very minimal at low single-scattering albedos, so that our model results tend to overestimate the reflectivity required to match the global average I/F . For the near-IR results we show the effect of changing from lambert (Minnaert exponent = 1) to zero limb darkening (Minnaert exponent = 1/2) for the August 1996 model. At $1 \mu\text{m}$ the difference between the two inferred single-scattering albedos is larger than the difference between various results in the CCD spectral range. Laboratory measurements by Lebofsky and Fegley (1976) and by Sill (1973) show that neither of the primary candidate cloud components (H_2S or NH_3) has an absorption feature that can explain the $0.6\text{--}0.7 \mu\text{m}$ dip in the inferred single-scattering albedo. While the pure frosts are relatively flat across the $0.3\text{--}1.03 \mu\text{m}$ spectral range, irradiated frosts do have a reflectance dip near $0.6 \mu\text{m}$. However, as noted by Baines *et al.* (1995), the fact that the irradiated frost remains highly reflective for $\lambda > 0.7 \mu\text{m}$ makes it a poor match to the observed cloud reflectivity.

The main new constraint we obtain is from our near-IR observations: if the 3.8-bar cloud is really present and opaque, it must have a very low single-scattering albedo at near-IR wavelengths, with a strong decrease between 1 and $1.2 \mu\text{m}$, to ~ 0.2 or possibly smaller. The upper limit shown as the dotted curve in Fig. 14, is obtained when the middle cloud (at 1.3 bars) is set to 0. The upper limits shown as points are from spatially resolved observations of the equatorial atmosphere, discussed in Paper III. The latter results are insensitive to limb-darkening uncertainties because they are derived from observations at small zenith angles. The exact value of the lower cloud single-scattering albedo in this spectral range is uncertain because of uncertain wavelength dependence in the properties of the middle cloud layer (at an effective pressure of 1.3 bars). Laboratory measurements of NH_3 frost reflectivity between 0.3 and $2.5 \mu\text{m}$ (Sill 1973) show large variations in reflectivity beyond $1 \mu\text{m}$, although it does not appear that the spectral features are compatible with our observations.

If the 3.8-bar cloud is partially transparent, then some of the inferred variation in single-scattering albedo might be due to wavelength dependence in the scattering efficiency. This is a more attractive mechanism to obtain decreasing reflectivity with wavelength than a strongly increased absorption by cloud

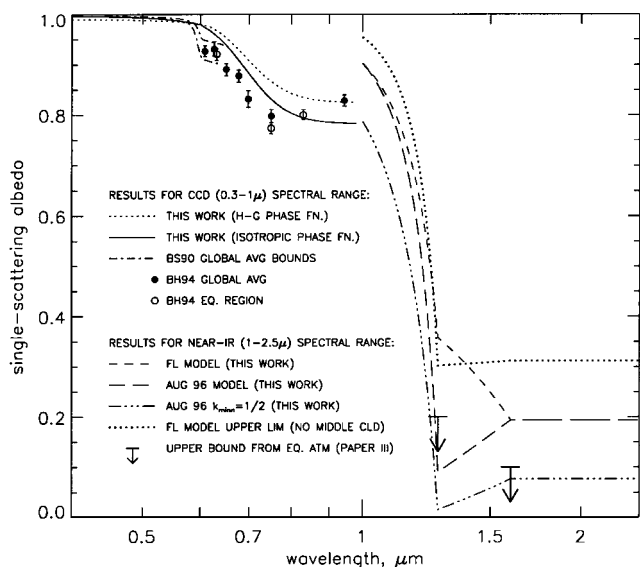


FIG. 14. Estimates of the single-scattering albedo of the 3.8-bar cloud particles, as a function of wavelength, assuming that the cloud is semi-infinite. Previous results are indicated by BS90 (Baines and Smith 1990) and BH94 (Baines and Hammel 1994). Our reflectivity results are converted to single-scattering albedo values as explained in the text. The FL Model is our model that fits the spectrum of Fink and Larson (1979).

particles, although it remains to be seen whether a semi-transparent cloud and size distribution can be found that will explain the reflectivity characteristics that have so far been inferred for the 3.8-bar cloud, including the transition at 0.6–0.7 μm , and the high reflectivity needed in the range 0.5–0.6 μm to match the moderate resolution CCD spectrum, as well as the H_2 quadrupole lineshape observed at high resolution. Near-IR spectral observations of Neptune at higher spectral resolution and at higher signal-to-noise ratios would be helpful in resolving the current ambiguities concerning relative contribution of lower and middle cloud layers.

Discussion: Modeling the outburst. On 15–16 March 1976, Joyce *et al.* (1977) measured unusually high values for Neptune's brightness, finding minimum magnitudes of 9.05 (J), 8.82 (H), and 9.61 (K). Our measurements on 13 August 1996 correspond to magnitudes of 10.23 (J), 10.1 (H), and 12.10 (K), implying that Neptune was brighter in 1976 by the rather large ratios of 3.1 (J), 3.25 (H), and 9.9 (K). If we simply multiply the upper level cloud amount in our 13 August model by a factor of 10 we obtain ratios that are comparable to these but a little too high for J and H. By using a slightly lower cloud-top pressure (89 mbars instead of 151 mbars) and using an upper cloud fraction 0.057 ($6.6\times$ the 13 Aug 96 value), the model brightness of Neptune for J, H, and K filters increases by factors of 2.84, 3.14, and 10.6, relative to 13 August, almost an exact fit to the Joyce *et al.* ratios. Thus, this major "outburst" on Neptune is consistent with the development of increased high-altitude cloud cover by a factor of ~ 7 relative to August 1996, but by only about a factor of ~ 2.5 relative to our model of the Fink and Larson (1979) observations, which were made during 28 Feb–2 March 1975, one year before the outburst. Narrowband filter measurements made the year following the outburst, also by Joyce *et al.* (1977), are roughly comparable to the Fink and Larson spectrum, and were interpreted by Pilcher (1977) as due to a planet-wide high-altitude reflecting layer. Our results suggest that it might also have been due to a collection of high-altitude discrete features.

6. SUMMARY AND CONCLUSIONS

Our main results can be summarized as follows:

(1) Disk-integrated albedo determinations of Neptune from WFPC2 imaging during 1994–1996, average about 4% lower at most wavelengths than the recent 1993 and 1995 groundbased spectra of Karkoschka (1994, 1998), probably mainly due to calibration differences. The difference equals the 4% absolute error quoted by Karkoschka. Near 0.89 μm the HST albedo values are a much more significant 15–29% lower than Karkoschka's values, a probable result of differences in the number and/or distribution of discrete bright cloud features during the different measuring periods.

(2) A Neptune lightcurve obtained from 13–14 August HST observations demonstrates the role of discrete bright cloud features in producing modulations at most wavelengths, confirm-

ing the previous results from other observing periods, and, for the first time, identified that a dark nonaxisymmetric south polar band was responsible for the modulation at blue wavelengths that was out of phase with the modulations at longer wavelengths, suggesting that dark features may also have played a significant role in variability seen in *b*-filter measurements the year following the 1986 peak in long-wavelength rotational modulation reported by Hammel *et al.* (1992).

(3) Models of the CCD spectrum using a linear combination of opaque heterogeneous or low-opacity reflecting layers at 100–150 mbars and 1.3 bars, overlying a 3.8-bar opaque reflector of spectrally varying albedo, match most of the observed spectral features in the 1993 Karkoschka (1994) spectrum within quoted relative measurement errors. With such a structure we find, as previously determined by Baines and Smith (1990) and Baines and Hammel (1994), that the putative H_2S cloud, at and below 3.8 bars, must exhibit a strong drop in reflectivity (and single-scattering albedo) at $\lambda \sim 0.6$, from near unity for $\lambda < 0.5 \mu\text{m}$ to ~ 0.24 (single-scattering albedo ~ 0.8) at 0.9 μm . The 1.3-bar effective cloud fraction was found to be $\sim 7\%$ at 0.55 μm , while the effective fractional coverage of upper tropospheric clouds (the highest layer) seems to have been about 1% at the time of Karkoschka's observations, and averages about 0.7% for our 1996 observations. These high-altitude clouds are the major source of rotational modulation within methane bands because of their heterogenous distribution and elevation above most of the methane absorption.

(4) Using IRTF observations, and fits to the shape of the F850LP lightcurve derived from the HST observations, we estimated rotational amplitudes for J, H, Spencer 1.7, and K filters of 0.14, 0.54, 0.86, and 1.2 mag respectively. These are compatible with lightcurve measurements in 1977 (Cruikshank 1978) but are considerably larger than seen in 1980 (Belton *et al.* 1981) during which multiple periods were observed and the J–K amplitude was ~ 0.5 mag.

(5) The disk-integrated albedos of Neptune that we derived at H–K wavelengths are factors of 2–7 less than the 1977 ground-based values of Fink and Larson (1979), which is consistent with reduced upper and mid-level cloud opacity in 1996. The upper cloud is found near the tropopause (124 ± 12 mbars in 1977 and 151 ± 13 mbars in 1996) with effective fractional coverage (or reflectivity) values of 2.3% in 1977, and 0.9 and 0.5% for 13 and 14 August 1996, respectively. Reflectivity at 1.3 bars (at $\lambda = 1 \mu\text{m}$) is found to be $\sim 4\%$ in 1977 and $\sim 1\%$ in 1996, although uncertainties about the wavelength dependence of 1.3- and 3.8-bar layers creates ambiguity about their relative values at near-IR wavelengths. A low 3.8-bar albedo is required in any case at 1.27 and 1.6 μm where we infer, from the Fink and Larson spectrum, upper limits of 0.05 and 0.045 respectively (corresponding single-scattering albedos are ~ 0.3 for both).

(6) A simple variation in upper cloud characteristics can reproduce the greatly increased brightness of Neptune during the major "outburst" in 1976. If we change the 13 August cloud model so that the upper cloud fractional coverage is increased to

~6% and the cloud-top pressure reduced from 151 to ~90 mbars, we are able to reproduce accurately the low J, H, and K magnitudes observed by Joyce *et al.* (1977) in March 1976, when Neptune was almost 10 times brighter in the K band than in 1996.

(7) Triton's disk-integrated albedo derived from HST imagery at 11 wavelengths from 0.25 to 0.9 μm are consistent, within error bars, with previous groundbased and *Voyager* measurements, including the low IUE result at 0.27 μm . We did not find evidence for the expected albedo decrease suggested by recent (1995 and 1997) observations of global warming on Triton (Elliot *et al.* 1998). The disk-integrated albedo of Triton in the range 1.2–2.4 μm , as determined from 1996 IRTF observations, is also consistent with previous 1991–1992 groundbased results of Cruikshank *et al.* (1993).

(8) A new determination of Triton's lightcurve from HST F467M and F547M filter observations during 1994–1996 show substantial deviations from *Voyager* models in the UV to long visible range. Although we find a minimum at roughly the same planetographic longitude on Triton (~100°), the 6–8% amplitude is about twice what Hillier *et al.* (1991) obtained at 560 nm.

(9) To derive calibrated near-IR groundbased observations of Neptune and Triton we developed refined analysis techniques. We measured encircled energy as a function of aperture for the IRTF NSFCAM observations, and developed a model to correct finite apertures for missing energy. Our review of solar spectral models, needed for I/F computation, determined that the Arvesen spectrum leads to significant errors in the range 1–2.5 μm , and made use of an improved spectral model by Kurucz (1994), an approach also taken by Colina *et al.* (1996). We also established that Triton can be used as a local photometric reference provided exposures are long enough to provide good signal-to-noise ratios.

APPENDIX A

IRTF Point Spread Functions

Understanding the PSF is an important element in deciding on photometric integrating apertures and on the size of the array used to characterize the PSF

for deconvolutions, and in carrying out simulations of IRTF observations. We consider diffraction, atmospheric turbulence, and a third component implied by the measurements, but the physical mechanism for which has not been unambiguously established.

Diffraction effects. According to Young (1974), the energy excluded from an aperture of radius r is given by $\epsilon(r) = \lambda/(5rD(1-d/D))$, where λ is the wavelength of light, D is the diameter of the primary mirror, d is the diameter of the secondary, and r is measured in radians. The IRTF values are $D = 3$ m, $d = 0.229$ m. For wavelengths of 1.26 to 2.4 μm , the minimum aperture diameter required to capture 99% of the diffracted energy varies from 3.7" to 7.1" (25 to 48 pixels, for the 0.1478 arcsec/pixel image scale). Apertures with diameters half these sizes would capture 98% of the diffracted energy, except for the very significant impact of two other effects that dominate the point spread function: atmospheric turbulence and scattering by telescope defects and dust.

Atmospheric effects on the PSF. The effects of atmospheric turbulence on a long-exposure image can be expressed in terms of the atmospheric transfer function

$$B(f) = \exp\left(-3.44(\lambda f/r_0)^{5/3}\right), \quad (12)$$

where f is angular frequency (inverse radians), and r_0 is defined as the telescope diameter at which diffraction and atmospheric turbulence have equal effects on telescope resolving power. The equation is derived assuming a Kolmogorov's turbulence spectrum (Roddier 1981). A two-dimensional Fourier transform of this spatial frequency transfer function yields the corresponding point spread function. Since $B(f)$ is nearly Gaussian (5/3 is near 6/3), the corresponding PSF is also nearly Gaussian, especially near the core, but in the wings the PSF falls off much more slowly than a Gaussian. The parameter r_0 is proportional to $\lambda^{6/5}$ and $\sec(z)^{3/5}$ (Walker 1987) so that the coefficient of $f^{5/3}$ in Eq. (12), which is a characteristic of the seeing only, can be written as $K(\lambda, z) = K(\lambda_0)(\lambda/\lambda_0)^{0.2}(\sec(z))^{0.6}$ where z is the solar zenith angle. The PSF is displayed in the subsequent discussion for a variety of seeing conditions.

Measured PSF profiles. To obtain a physical understanding of the dependence of integral value on enclosed radius, we determined averaged brightness profiles for each of three seeing conditions. Our primary measurements were integrations of point-source energy over a range of apertures, correcting for background by subtracting the average background obtained from an annulus 1.3 to 1.7 times the radius of the largest integrating aperture. We stopped the integrations at 30 pixels radius (4.4"), using background averages from 39 to 51 pixels. In the range 0.3"–4.4" we obtained the average intensity profiles by differentiation. These profiles were averaged over 7–9 images for each seeing group. For the inner core of the brightness profiles we used Gaussian fits to representative images. The J-filter brightness profile results for three different seeing conditions are displayed in Fig. 15. The uncertainties in the radial profiles are

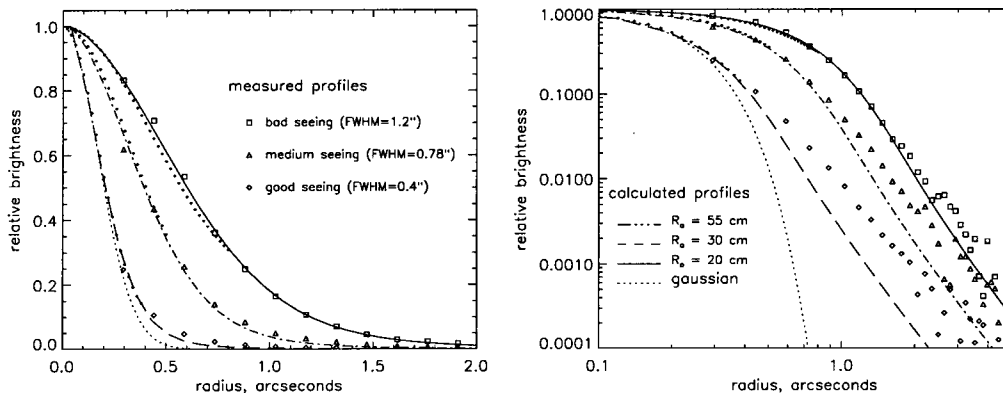


FIG. 15. Linear (left) and logarithmic (right) J-filter radial brightness profiles for good, fair, and poor seeing conditions, compared to model atmospheric PSFs derived from Eq. (12) using r_0 values of 20, 30, and 55 cm, which provide approximate fits to the core region of each profile (see text for discussion). The Gaussian profile (dotted curve in right panel) falls off much more rapidly than either the model PSF or the observations.

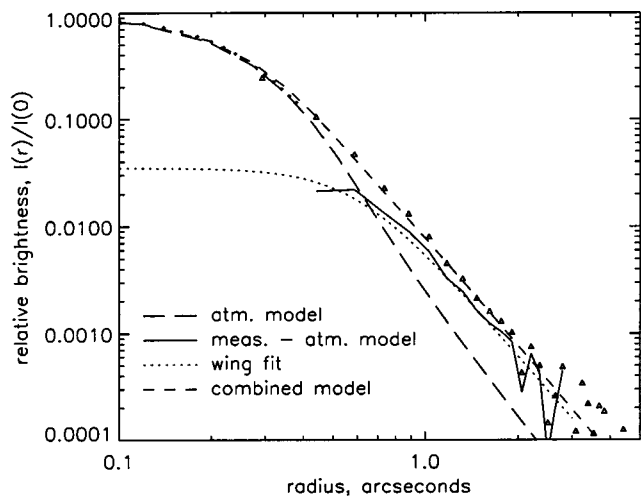


FIG. 16. Model of a J-filter radial brightness profile, consisting of an atmospheric seeing component (long dashes) and a wing component (dotted), compared to measurements (triangles).

relatively small, except for the normalization constant, which has been adjusted to give approximate agreement between the core profile and the ensemble average profile for each seeing group. The Gaussian profile can be seen to decline much more rapidly with radius than the observed profiles. Fourier transform reference seeing profiles are also shown, for r_0 values that provide an approximate best fit to the cores of the observed profiles. These also fall below the measured intensities at large radii. This is more apparent for the best seeing, because the PSF component due to atmospheric effects is concentrated at smaller angles.

As shown in Fig. 16, the wing can be empirically modeled with a simple function that falls off approximately as $1/r^{3.25}$. The plotted function, which approximately fits the difference between the observations and the atmospheric PSF model, has the form $I_w(r) = a/(1 + (r/b)^{3.25})$, and fit parameter values $a = 0.035''$ and $b = 0.6''$. The area integral of this function is approximately $2\pi ab^2$, which evaluates to 0.079 arcsec^2 (assuming a dimensionless brightness). For comparison, the integral of the main atmospheric component is only 0.196 arcsec^2 (2.48 times larger). Thus, the wing contribution is $0.079/0.275 = 29\%$, while the main atmospheric component of the PSF contributes the remaining 71%. The justification for assuming the wing contribution is flat near $r = 0$ comes from the likely physical mechanism that produces it. In reference to measurements of stellar profiles, Kormandy (1973) pointed out that the only viable explanation for power-law wing contributions is scattering by dust and defects on the telescope mirror. These features would have to be larger than $\lambda/(2\pi r)$ in order to produce a falloff of intensity beyond radius r . For $r = 1''$ the defects would have to be about 4 cm or larger, clearly well beyond the range of dust particles, unless particles within the camera optics are responsible. If diffraction from particles or defects are responsible, the scattering function will consist of overlapping single-particle scattering functions of the form $I(r) = \frac{1}{4\pi} x^2 \left(\frac{2}{xr} J_1(xr)\right)^2$, where J_1 is the Bessel function of order 1, and $x = 2\pi a/r$, where a is the particle (or defect) radius. Near $r = 0$, $I(r)$ approaches a constant value of $\pi a^2/\lambda^2$, and thus we made use of a function of similar characteristics in modeling the wing behavior.

APPENDIX B

Solar Irradiance Standards

In defining the geometric albedo of planetary bodies and their features, it is necessary to determine not only the flux reflected by the body, but also the incident flux from the Sun. To compute the incident solar flux average within each relevant filter passband, we initially used the solar irradiance spectrum compiled by Wehrli (1985), which is based on Brasseur and Simon (1981) for the region 200–310 nm, Arvesen *et al.* (1969) for 310–330 nm, Neckel

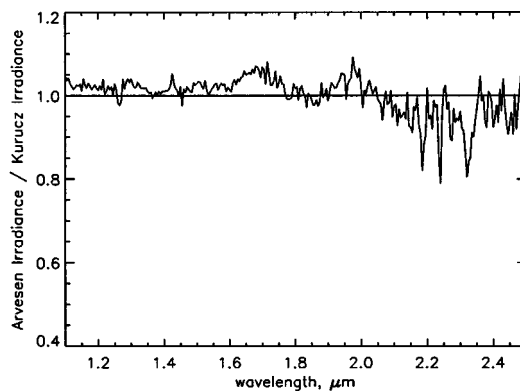


FIG. 17. Ratio of measured solar spectrum of Arvesen *et al.* (1969) to recent detailed solar model spectrum of Kurucz (1994).

and Labs (1984) for the region 330–869 nm, and Smith and Gottlieb (1974) and Arvesen *et al.* (1969) for wavelengths beyond 869 nm. Wehrli adjusted the Arvesen *et al.* (1969) measurements to fit the continuum values of Neckel and Labs (1984), and Labs and Neckel (1970). After further adjustments to match joints between the various spectral contributions, the total spectrum was scaled to yield a solar constant of 1367 W/m^2 . Aside from a few flaws in the matching and interpolation process, the main problem with this compilation is a result of significant spectral structure in the Arvesen *et al.* spectrum that is not due to solar absorption lines. This can best be seen by comparing the Arvesen spectrum to a detailed solar model spectrum developed by Kurucz (1994). The ratio, shown in Fig. 17, is full of structure that is almost entirely due to the Arvesen measurements, which appear to have significant telluric contamination in this range. This was also pointed out by Gao and Green (1995) who noted the defects in the World Radiation Center spectrum compiled by Wehrli (1985). The same problems were noted by Colina *et al.* (1996), who decided to use the Kurucz model spectrum for the region 0.96–2.5 μm in compiling a reference spectrum for NICMOS calibration.

In computing solar flux integrals over the K-filter passband, we obtain from Arvesen's spectrum a value that is nearly 8% smaller than we obtain using the Kurucz spectrum. This translates into an 8% error in albedo, and because of the large variations within this band, CVF calibration errors can be up to twice as large as those of the wide band observations. By using the Kurucz spectrum we reduced the discrepancy between our own narrowband and broadband measures of geometric albedo in this spectral range, further validating the conclusion that the Arvesen spectrum is not correct in this spectral region. Thus we used Kurucz (1994) for the range 1–2.5 μm .

The ratio of our compiled spectrum to the Kurucz model for the region 200 nm to 1 μm is provided in Fig. 18. Because the Kurucz model is fitted to

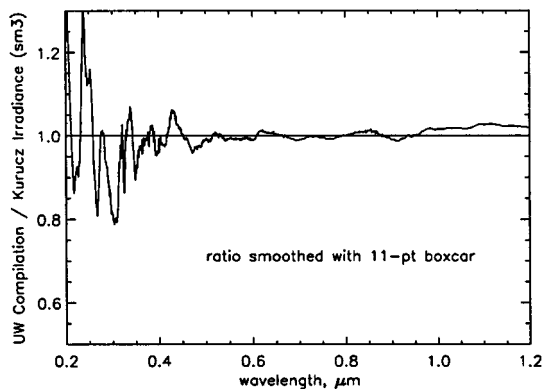


FIG. 18. Ratio of our composite solar irradiance spectrum to the recent detailed solar model spectrum of Kurucz (1994).

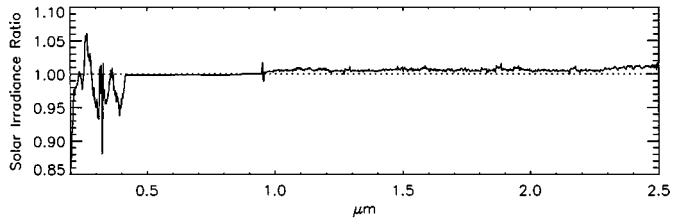


FIG. 19. Ratio of our composite solar irradiance spectrum to the recent compilation by Colina *et al.* (1996).

Neckel and Labs and apparently Labs and Neckel, which is also the basis for our compilation in the range 330–869 nm, the relatively good agreement there is to be expected. There are disagreements at shorter wavelengths however. Comparing our reference spectrum to the Colina *et al.* (1996) compilation (Fig. 19), we see a comparable disagreement at short wavelengths. The difference arises mainly from source differences: in contrast to the sources mentioned earlier, Colina *et al.* (1996) used Woods *et al.* (1996) up to 410 nm. We agree very closely with Colina *et al.* at longer wavelengths, generally to better than 1%, which is to be expected because we used the same sources. Small differences at wavelengths longer than 0.95 μm are apparently due to differences in binning and normalizing the Kurucz model spectrum. In future analyses we plan to use the Colina *et al.* compilation.

ACKNOWLEDGMENTS

This work is based on observations with the NASA/ESA Hubble Space Telescope, obtained at the Space Telescope Science Institute, which is operated by the Association of Universities for Research in Astronomy, Inc., under NASA Contract NAS5-26555. We thank Support Astronomer Keith Noll and Program Coordinator Denise Taylor, who provided excellent assistance in designing the HST observing sequence. We also made use of observations obtained at the NASA Infrared Telescope Facility, operated for NASA by University of Hawaii Institute for Astronomy. Support for this work was provided by NASA through Space Telescope Science Institute Grants AR-06374.01-95A and GO-06650.01-95A, and through the Planetary Astronomy Program, under Grant NAG5-6788, and Visiting Astronomer support by the IRTF. We are grateful for the excellent support provided by IRTF astronomer Bob Greene and telescope operator Lars Berkgnut, and to IRTF director Bob Joseph for his efforts in arranging the observing schedule to coincide with the HST observations. We thank Heidi Hammel and an anonymous reviewer for extensive and helpful comments.

REFERENCES

- Arvesen, J. C., R. N. Griffin, Jr., and B. D. Pearson, Jr. 1969. Determination of extraterrestrial solar spectral irradiance from a research aircraft. *Appl. Opt.* **8**, 2215–2232.
- Baggett, S., and S. Gonzaga 1998. WFPC2 long-term photometric stability. Instrument Science Report WFPC2 98–03 available from the Space Telescope Science Institute (stsci.edu).
- Baines, K. H., and H. B. Hammel 1994. Clouds, hazes, and the stratospheric methane abundance in Neptune. *Icarus* **109**, 20–39.
- Baines, K. H., and W. H. Smith 1990. The atmospheric structure and dynamical properties of Neptune derived from ground-based and IUE spectrophotometry. *Icarus* **85**, 65–108.
- Baines, K. H., H. B. Hammel, K. A. Rages, P. N. Romani, and R. E. Samuelson 1995. Clouds and hazes in the atmosphere of Neptune. In *Neptune and Triton* (D. P. Cruikshank, M. S. Matthews, and A. M. Schumann, Eds.), pp. 489–546. Univ. of Arizona Press, Tucson.
- Belton, M. J. S., L. Wallace, and S. Howard 1981. The periods of Neptune: Evidence for atmospheric motions. *Icarus* **45**, 263–273.
- Bergstralh, J. T., and K. H. Baines 1984. Properties of the upper troposphere of Uranus and Neptune derived from observations at “visible” to near-infrared wavelengths. In *Uranus and Neptune* (J. Bergstralh, Ed.), NASA CP 2330, pp. 179–212.
- Blackwell, D. E., S. K. Leggett, A. D. Petford, C. M. Mountain, and M. J. Selby 1983. Absolute calibration of the infrared flux from Vega at 1.24, 2.20, 3.76, and 4.6 μm by comparison with a standard furnace. *Mon. Not. R. Astron. Soc.* **205**, 897–905.
- Brasseur, G., and P. Simon 1981. Stratospheric chemical and thermal response to long-term variability in solar UV irradiance. *J. Geophys. Res.* **86**, 7343.
- Brown, R. H., D. P. Cruikshank, and D. Griep 1985. Temperature of Comet IRAS–Araki–Alcock 1983d. *Icarus* **62**, 273–281.
- Brown, R. H., D. P. Cruikshank, J. Veverka, P. Helfenstein, and J. Eluszkiewicz 1995. Surface composition and photometric properties of Triton. In *Neptune and Triton* (D. P. Cruikshank, M. S. Matthews, and A. M. Schumann, Eds.), pp. 991–1030. Univ. of Arizona Press, Tucson.
- Buratti, B. J., J. Goguen, J. Gibson, and J. Mosher 1994. Historical photometric evidence for volatile migration on Triton. *Icarus* **110**, 303–314.
- Casali, M. M., and T. G. Hawarden 1992. *JCMT-UKIRT Newsletter*, No. 3, August issue, p. 33.
- Cohen, M., R. G. Walker, M. J. Barlow, and J. R. Deacon 1992. Spectral irradiance calibration in the infrared. I. Ground-based and IRAS broadband calibrations. *Astron. J.* **104**, 1650–1657.
- Colina, L., R. C. Bohlin, and F. Castelli 1996. The 0.12–2.5 μm absolute flux distribution of the Sun for comparison with solar analog stars. *Astron. J.* **112**, 307–315.
- Cruikshank, D. P. 1978. On the rotation period of Neptune. *Astrophys. J.* **220**, L57–L59.
- Cruikshank, D. P. 1985. Variability of Neptune. *Icarus* **64**, 107–111.
- Cruikshank, D. P., T. L. Roush, T. C. Owen, T. R. Geballe, C. de Bergh, B. Schmitt, R. H. Brown, and J. J. Bartholomew 1993. Ices on the surface of Triton. *Science* **261**, 742–745.
- Davies, M., V. K. Abalakin, A. Brahic, M. Bursa, B. H. Chovitz, J. K. H. Lieske, P. K. Seidelmann, A. T. Sinclair, and I. S. Tiufin 1992. Report of the IAU/IAG/COSPAR Working Group on cartographic coordinates and rotational elements of the planets and satellites—1991. *Celest. Mech. Dynam. Astron.* **53**, 377–397.
- Dyck, H. M., G. T. van Belle, and R. R. Thompson 1998. Radii and effective temperatures for K and M giants and supergiants. II. *Astron. J.* **116**, 981–986.
- Elliot, J. L., H. B. Hammel, L. H. Wasserman, O. G. Franz, S. W. McDonald, M. J. Person, C. B. Olkin, E. W. Dunham, J. R. Spencer, J. A. Stansberry, M. W. Buie, J. M. Pasachoff, B. A. Babcock, and T. H. McConnochie 1998. Global warming on Triton. *Nature* **393**, 765–767.
- Engels, D., W. A. Sherwood, W. Wamsteker, and G. V. Schultz 1981. Infrared observations of southern bright stars. *Astron. Astrophys. Suppl. Ser.* **45**, 5–9.
- Fink, U., and S. Larson 1979. The infrared spectra of Uranus, Neptune, and Titan from 0.8 to 2.5 microns. *Astrophys. J.* **233**, 1021–1040.
- Gao, B., and R. O. Green 1995. Presence of terrestrial atmospheric gas absorption bands in standard extraterrestrial solar irradiance curves in the near-infrared spectral region. *Appl. Opt.* **34**, 6263–6268.
- Gouguen, J. D., H. B. Hammel, and R. H. Brown 1989. V photometry of Titania, Oberon, and Triton. *Icarus* **77**, 239–247.
- Grundy, W. H., and U. Fink 1991. A new spectrum of Triton near the time of the Voyager encounter. *Icarus* **93**, 379–385.
- Hammel, H. B., N. L. Lark, M. Rigler, and T. J. Kreidl 1989. Disk-integrated photometry of Neptune at methane-band and continuum wavelengths. *Icarus* **79**, 1–14.

- Hammel, H. B., S. L. Lawson, J. Harrington, G. W. Lockwood, D. T. Thompson, and C. Swift 1992. An atmospheric outburst on Neptune from 1986 through 1989. *Icarus* **99**, 363–367.
- Hansen, J. E., and L. D. Travis 1974. Light scattering in planetary atmospheres. *Space Sci. Rev.* **16**, 527–610.
- Hillier, J., P. Helfenstein, A. Verbiscer, J. Veverka, R. H. Brown, J. Goguen, and T. V. Johnson 1990. Voyager disk-integrated photometry of Triton. *Science* **250**, 419–421.
- Hillier, J., J. Veverka, P. Helfenstein, and A. McEwen 1991. The wavelength dependence of Triton's light curve. *J. Geophys. Res.* **96**, 19,211–19,215.
- Holtzman, J. A., C. J. Burrows, S. Casertano, J. J. Hester, J. T. Trauger, A. M. Watson, and G. Worthey 1995. The photometric performance and calibration of WFPC2. *Publ. Astron. Soc. Pacific* **107**, 1065–1093.
- Joyce, R. R., C. B. Pilcher, D. P. Cruikshank, and D. Morrison 1977. Evidence for weather on Neptune, I. *Astrophys. J.* **214**, 657–662.
- Karkoschka, E. 1994. Spectrophotometry of the jovian planets and Titan at 300- to 1000-nm wavelength: The methane spectrum. *Icarus* **111**, 174–192.
- Karkoschka, E. 1998. Methane, ammonia, and temperature measurements of the jovian planets and Titan from CCD-spectrophotometry. *Icarus* **133**, 134–146.
- Kormandy, J. 1973. Calibration of direct photographs using brightness profiles of field stars. *Astron. J.* **78**, 255–262.
- Kurucz, R. L. 1994. Synthetic infrared spectra. In *Infrared Solar Physics* (D. M. Rabin, J. T. Jefferies, and C. Lindsey, Eds.), pp. 523–531. Kluwer Academic, Dordrecht.
- Labs, D., and H. Neckel 1970. Transformation of the absolute solar radiation data into the "International practical temperature scale of 1968." *Solar Phys.* **15**, 79–87.
- Lark, N. L., H. B. Hammel, D. P. Cruikshank, D. P. Tholen, and M. A. Rigler 1989. The brightness and light-curve of Triton in 1987. *Icarus* **79**, 15–22.
- Lebofsky, L. A., and M. B. Fegley, Jr. 1976. Laboratory reflection spectra for the determination of chemical composition of icy bodies. *Icarus* **28**, 379–387.
- Lockwood, G. W., and D. T. Thompson 1991. Solar cycle relationship clouded by Neptune's sustained brightness maximum. *Nature* **344**, 593–594.
- Lockwood, G. W., D. T. Thompson, H. B. Hammel, P. Birch, and M. Candy 1991. Neptune's cloud structure in 1989: Photometric variations and correlation with groundbased imaging. *Icarus* **90**, 299–307.
- Neckel, H., and D. Labs 1984. The solar radiation between 3300 and 12500 Å. *Solar Phys.* **90**, 205–258.
- Neff, J. S., D. C. Humm, and J. T. Bergstralh 1984. Absolute spectrophotometry of Titan, Uranus, and Neptune: 3500–10,500 Å. *Icarus* **60**, 221–235.
- Nelson, R. M., B. J. Buratti, B. D. Wallis, W. D. Smythe, L. J. Horn, A. L. Lane, and M. J. Mayo 1990. Spectral geometric albedo and bolometric bond albedo of Neptune's satellite Triton from Voyager observations. *Geophys. Res. Lett.* **17**, 1761–1764.
- Pilcher, C. B., 1977. Evidence for weather on Neptune. II. *Astrophys. J.* **214**, 663–666.
- Pryor, W. R., R. A. West, K. E. Simmons, and M. Delitsky 1992. High-phase angle observations of Neptune at 2650 Å and 7500 Å: Haze structure and particle properties. *Icarus* **99**, 302–316.
- Rodder, F. 1981. The effects of atmospheric turbulence in optical astronomy. In *Progress in Optics XIX* (E. Wolf, Ed.), pp. 281–376. North-Holland, Amsterdam.
- Sill, G. T. 1973. Reflection spectra of solids of planetary interest. *Comm. Lunar Planet. Lab.* **10**, 1.
- Smith, E. V. P., and D. M. Gottlieb 1974. Solar flux and its variations. *Space Sci. Rev.* **16**, 771–802.
- Smith, B. A., L. A. Soderblom, D. Banfield, C. Barnet, A. T. Basilevsky, R. F. Beebe, K. Bollinger, J. M. Boyce, A. Brahic, G. A. Briggs, R. H. Brown, C. Chyba, S. A. Collins, T. Colvin, A. F. Cook, II, D. Crisp, S. K. Croft, D. Cruikshank, J. N. Cuzzi, G. E. Danielson, M. E. Davies, E. DeJong, L. Dones, D. Godfrey, J. Gougen, J. Grenier, V. R. Haemmerle, H. Hammel, C. J. Hansen, C. P. Helfenstein, C. Howell, G. E. Hunt, A. P. Ingersoll, T. V. Johnson, J. Kargel, R. Kirk, D. I. Kuehn, S. Limaye, H. Masursky, A. McEwen, D. Morrison, T. Owen, W. Owen, J. B. Pollack, C. C. Porco, K. Rages, P. Rogers, D. Rudy, C. Sagan, J. Schwartz, E. M. Shoemaker, M. Showalter, B. Sicardy, D. Simonelli, J. Spencer, L. A. Sromovsky, C. Stoker, R. G. Strom, V. E. Suomi, S. P. Synnot, R. J. Terrile, P. Thomas, W. R. Thompson, A. Verbiscer, and J. Veverka 1989. Voyager 2 at Neptune: Imaging science results. *Science* **246**, 1422–1454.
- Space Telescope Science Institute 1996. *Wide Field and Planetary Camera 2 Instrument Handbook*. Version 4.0. Space Telescope Science Institute, Baltimore, MD.
- Spencer, J. R., and J. M. Moore 1992. The influence of thermal inertia on temperatures and frost stability on Triton. *Icarus* **99**, 261–272.
- Sromovsky, L. A., P. M. Fry, S. S. Limaye, K. H. Baines, and T. Dowling 1998. HST and IRTF observations of Neptune during 1998. *Bull. Am. Astron. Soc.* **30**, 1098.
- Sromovsky, L. A., P. M. Fry, K. H. Baines, S. S. Limaye, T. E. Dowling, and G. S. Orton 2001a. Coordinated 1996 HST and IRTF Imaging of Neptune and Triton. I. Observations, navigation, and deconvolution techniques. *Icarus* **149**, 416–434.
- Sromovsky, L. A., P. M. Fry, T. E. Dowling, K. H. Baines, and S. S. Limaye 2001b. Coordinated 1996 HST and IRTF Observations of Neptune and Triton III: Neptune's atmospheric circulation and cloud structure. *Icarus* **149**, 459–488.
- Stern, S. A., T. E. Skinner, N. Brosch, J. van Santvoort, and L. Trafton 1989. The first UV spectrum of Triton: IUE Observations 2600–3200 Å. *Astrophys. J.* **342**, 1115.
- Voit, M. 1997. *HST Data Handbook, Vol. 1, Current Instruments, Vers. 3*. Space Telescope Science Institute, Baltimore MD.
- Walker, G. 1987. *Astronomical Observations*. Cambridge Univ. Press, New York.
- Wehrli, Ch. 1985. WRC Reference Spectrum. PMOD Publication 615. Meteorological Observatory at Davos, Switzerland.
- Whitmore, B., I. Heyer, and S. Casertano 1999. Charge-transfer efficiency of WFPC2. *Publ. Astron. Soc. Pacific* **111**, 1559–1576.
- Woods, T. N., D. K. Prinz, G. J. Rottman, J. London, P. C. Crane, R. P. Cebula, E. Hilsenrath, G. E. Brueckner, M. D. Andrews, O. R. White, M. E. Van-Hoosier, L. E. Floyd, L. C. Herring, B. G. Knapp, C. K. Pankratz, and P. A. Reiser 1996. Validation of the UARS solar ultraviolet irradiances: Comparison with the ATLAS 1 and 2 measurements. *J. Geophys. Res.* **101**, 9541–9569.
- Yelle, R. V., J. I. Lunine, J. B. Pollack, and R. H. Brown 1995. Lower atmospheric structure on Triton. In *Neptune and Triton* (D. P. Cruikshank, M. S. Matthews, and A. M. Schumann, Eds.), pp. 1031–1105. Univ. of Arizona Press, Tucson.
- Young, A. T. 1974. Observational techniques and data reduction. In *Methods of Experimental Physics* (N. Carleton, Ed.), Vol. 12A, pp. 123–192. Academic Press, New York.